

Design of customized coronavirus receptors

<https://doi.org/10.1038/s41586-024-08121-5>

Received: 4 March 2024

Accepted: 25 September 2024

Published online: 30 October 2024



Peng Liu^{1,7}, Mei-Ling Huang^{1,7}, Hua Guo^{2,7}, Matthew McCallum^{3,7}, Jun-Yu Si¹, Yuan-Mei Chen¹, Chun-Li Wang¹, Xiao Yu¹, Lu-Lu Shi¹, Qing Xiong¹, Cheng-Bao Ma¹, John E. Bowen³, Fei Tong¹, Chen Liu¹, Ye-hui Sun¹, Xiao Yang¹, Jing Chen², Ming Guo¹, Jing Li¹, Davide Corti⁴, David Veesler^{3,5}✉, Zheng-Li Shi^{2,6}✉ & Huan Yan¹✉

Although coronaviruses use diverse receptors, the characterization of coronaviruses with unknown receptors has been impeded by a lack of infection models^{1,2}. Here we introduce a strategy to engineer functional customized viral receptors (CVRs). The modular design relies on building artificial receptor scaffolds comprising various modules and generating specific virus-binding domains. We identify key factors for CVRs to functionally mimic native receptors by facilitating spike proteolytic cleavage, membrane fusion, pseudovirus entry and propagation for various coronaviruses. We delineate functional SARS-CoV-2 spike receptor-binding sites for CVR design and reveal the mechanism of cell entry promoted by the N-terminal domain-targeting S2L20-CVR. We generated CVR-expressing cells for 12 representative coronaviruses from 6 subgenera, most of which lack known receptors, and show that a pan-sarbecovirus CVR supports propagation of a propagation-competent HKU3 pseudovirus and of authentic RsHuB2019A³. Using an HKU5-specific CVR, we successfully rescued wild-type and ZsGreen-HiBiT-incorporated HKU5-1 (LMH03f) and isolated a HKU5 strain from bat samples. Our study demonstrates the potential of the CVR strategy for establishing native receptor-independent infection models, providing a tool for studying viruses that lack known susceptible target cells.

The *Coronaviridae* family encompasses hundreds of viruses categorized into four genera: alphacoronaviruses, betacoronaviruses, gammacoronaviruses and deltacoronaviruses. Human betacoronaviruses have caused three significant outbreaks in the twenty-first century, highlighting the zoonotic risks associated with animal coronaviruses that are not well characterized, which primarily infect bats^{3,4}.

Coronavirus entry into target cells is mediated by the trimeric spike glycoprotein^{5–7} (S), which can remain intact or undergo cleavage at the S₁/S₂ cleavage site, yielding S₁ and S₂ subunits⁷. The S₁ subunit engages specific receptors, leading to conformational changes that trigger membrane fusion mediated by the S₂ subunit. Activation of the S₂ fusion machinery leads to exposure and proteolysis of the S₂' cleavage site situated immediately upstream of the fusion peptide and large-scale conformational changes from the prefusion conformation to the post-fusion conformation. Except for mouse hepatitis virus (MHV), most coronaviruses use the C-terminal domain (CTD)—also known as domain B—of the S₁ subunit as receptor-binding domain (RBD), adopting either ‘down’ or ‘up’ conformations⁸, with the up state enabling receptor engagement^{8,9}. SARS-CoV-2 spike recognizes the protease (head) domain of human angiotensin-converting enzyme 2 (ACE2) through its receptor-binding motif (RBM). ACE2-induced conformational changes expose the S₂' site, promoting proteolytic cleavage by cell surface TMPRSS2, endosomal cathepsin L or other proteases¹⁰.

There are five widely acknowledged protein entry receptors for coronaviruses: ACE2, APN, DPP4, CEACAM1a and TMPRSS2^{2,11,12}. ACE2 is an entry receptor for various coronaviruses, including NL63, SARS-CoV-1, SARS-CoV-2 and several clades of bat-borne sarbecoviruses and merbecoviruses^{13–16}. Cryo-electron microscopy (cryo-EM) analysis of human ACE2 (hACE2) shows that it exists as a dimer, with direct engagement of the head domain by the RBD of SARS-CoV-2 spike, particularly the α1- and α2-helices and the loop connecting the β3- and β4-sheets⁹. However, the contribution of other regions of ACE2 to receptor function remains unknown. Several alternative receptors or coreceptors for SARS-CoV-2 have been reported, but their entry-supporting efficiencies are generally low compared with that of ACE2^{17,18}. Many bat coronaviruses have no known receptors, thus limiting our ability to study them and to develop countermeasures¹⁴.

Functional entry receptors are crucial for developing infection models and inhibition assays, and identifying native receptors is time-consuming with no guarantee of success. To address this unmet need, an alternative approach of establishing infection models independently of the presence of native receptors is awaiting exploration; such an approach has been carried out for MHV¹⁹. The design of functional coronavirus receptors is impeded by the lack of knowledge regarding the critical sequence and structural requirements to induce spike conformational changes leading to cell entry. Studies that focus on SARS-CoV-2 or Middle East respiratory syndrome coronavirus (MERS-CoV) have identified distinct mechanisms of

¹State Key Laboratory of Virology, College of Life Sciences, TaiKang Center for Life and Medical Sciences, Wuhan University, Wuhan, China. ²Key Laboratory of Virology and Biosafety, Wuhan Institute of Virology, Chinese Academy of Sciences, Wuhan, China. ³Department of Biochemistry, University of Washington, Seattle, WA, USA. ⁴Humabs BioMed SA, subsidiary of Vir Biotechnology, Bellinzona, Switzerland. ⁵Howard Hughes Medical Institute, University of Washington, Seattle, WA, USA. ⁶Guangzhou Laboratory, Guangzhou International Bio Island, Guangzhou, China. ⁷These authors contributed equally: Peng Liu, Mei-Ling Huang, Hua Guo, Matthew McCallum. [✉]e-mail: dveesler@uw.edu; zlshi@wh.iov.cn; huayan@whu.edu.cn

ACE2- or DPP4-independent entry in vitro, via alternative receptors, antibody-dependent Fc_YR-mediated entry or membrane-anchored antibodies, in either a productive or a nonproductive manner^{20–23}. These findings indicate that the interactions between coronaviruses and cognate receptors are dispensable for entry, making it possible to design receptors without prior knowledge of the native receptors.

In this study, we built receptors with customized specificity by grafting virus-binding domains (VBDs) on various transmembrane scaffolds, and demonstrate that ACE2 can be entirely substituted to promote sarbecovirus entry into cells. By identifying the key factors that affect receptor functionality, we developed a generally applicable modular design strategy to build functional CVRs that support productive viral entry and demonstrate the strengths of this strategy for various applications in virology.

Modular design of CVR

To understand the contribution of different domains of hACE2 to its receptor function, we first assessed whether we could replace the hACE2 head domain with a computationally designed SARS-CoV-2-targeting miniprotein while maintaining its receptor function. We created four hACE2 chimeric proteins, replacing the head domain or the head and neck domains with a previously reported miniprotein, LCB1 or LCB3²⁴. Using authentic SARS-CoV-2 infection assays, we demonstrated that these chimeric proteins effectively supported viral infection (Extended Data Fig. 1a,b).

These modified receptors maintained binding efficiency to SARS-CoV-2 RBD even as the remaining ACE2 sequences were removed (Fig. 1a–c). However, their ability to promote pseudovirus entry decreased concurrently with the shortening of the ACE2 anchor. The shortest 132-amino-acid protein maintained detectable receptor function, but at a much lower level than full-length ACE2 (approximately 0.5%; Fig. 1d,e and Supplementary Table 1). We subsequently designed modified receptors comprising parts from other viral or immune receptors (R1–R4), along with the addition of a receptor endocytosis-prevention motif (EPM) to enhance surface distribution²⁵ (R5) (Fig. 1f). All of the chimeric receptors showed good expression in HEK293T cells and bound efficiently to the RBD (Fig. 1g,h). In particular, the chimeric protein with the ACE2 anchor substituted with triple (3×) 23-amino-acid tandem repeats (TR23) from CLEC4M or human IgG Fc (hFc) supported efficient entry (Fig. 1i,j). Further substituting the remaining sequences with corresponding IL2R- α sequences maintained similar entry efficiency, suggesting that all of ACE2 is replaceable (Fig. 1i,j). Among 31 tested transmembrane segments and several cytosolic domains from various receptors, the transmembrane and cytosolic domain (TMC) from MXRA8 resulted in the highest entry efficiency (Extended Data Fig. 1c–h and Supplementary Table 2). Constructs with an EPM showed improved cell surface localization and improved entry-supporting efficiency (Fig. 1i,j and Extended Data Fig. 1i,j).

Moreover, constructs with a type II transmembrane topology efficiently supported SARS-CoV-2 and MERS-CoV entry, indicating the feasibility of generating receptors with different transmembrane topologies (Extended Data Fig. 2a,b). We then explored the effect of spacer length and oligomerization on receptor function by testing spacers with various numbers of TR23 tandem repeats or immunoglobulin-like domains from human IgG or mouse CEACAM1a (Fig. 1k,l and Extended Data Fig. 2c–i). The results indicated that the triple TR23, two immunoglobulin domains or two immunoglobulin-like domains represent the optimal spacers, and abolishing dimerization using Fc mutants has no significant effect on receptor function²⁶ (Fig. 1m and Extended Data Fig. 2c–i).

Different types of SARS-CoV-2 RBD-targeting VBDs were tested for receptor grafting, including designed helical frameworks, designed

ankyrin repeat proteins (DARPins), nanobodies, single-chain variable fragments (scFvs) and Fab (Extended Data Fig. 2j,m). All of these VBD types were functional, with nanobodies being preferred owing to their relatively small size, single-chain nature and compatibility with biopanning (Extended Data Fig. 2k,l,n,o). We also demonstrated the functionality of a bispecific receptor carrying two VBDs of different specificity and tandem trimeric VBDs (Extended Data Fig. 3a–f) and facilitation of viral entry by soluble receptor adapters that connect viral RBD and ACE2 or Fc_YRIIa, respectively (Extended Data Fig. 3g–l). By contrast, soluble antibodies without membrane anchoring ability were unable to efficiently promote viral entry, even when viruses were pre-attached to the cells (Extended Data Fig. 3m–o).

We further demonstrated functionality of CVRs compared with ACE2 through a series of experiments showing membrane fusion, authentic SARS-CoV-2 infection and virus specificity in different cell types (Extended Data Fig. 4a–e). The entry-promoting efficiencies of CVRs were markedly superior to those of several documented SARS-CoV-2 alternative receptors, coreceptors, entry factors or binding proteins¹⁷ (Extended Data Fig. 4f).

Thus, we proposed a modular design strategy for generating CVRs comprising the customized VBD and modularized artificial receptor scaffolds (ARSSs) that support coronavirus entry with efficiency similar to that of native receptors (Fig. 1n).

Mapping of functional CVR epitopes

In our initial exploration of the relationship between CVR function and binding affinity or neutralizing activity, we evaluated 25 neutralizing nanobodies that target the SARS-CoV-2 RBD²⁷. However, we did not find a clear link between entry-supporting ability and binding affinity or neutralizing activity. These results suggest that there are other important factors for CVR function, and in particular, binding to epitopes that are not clearly defined for these 25 nanobodies (Extended Data Fig. 5 and Supplementary Table 2).

We engineered CVRs with scFvs derived from 22 well-characterized SARS-CoV-2-neutralizing antibodies covering a wide range of neutralizing epitopes^{28–35} (Fig. 2a). These antibodies were converted to scFv-based VBDs with an N-terminal heavy chain (HL) or N-terminal light chain (LH), resulting in 44 CVRs (Fig. 2b). All CVRs exhibited good expression in our system and bound efficiently to the SARS-CoV-2 spike trimer, except for 76E1, which recognizes a conformationally masked epitope, which is exposed after receptor binding^{33,36} (Extended Data Fig. 6a,b). The scFv-CVRs that recognize epitopes close to the canonical RBM (sites i, ii and iii) and many CVRs that recognize the RBD core domain supported efficient entry³⁷ (Fig. 2c). However, a subset of RBD epitopes were not suitable for CVR design, such as those recognized by S309 and two other antibodies that bind to a quaternary epitope spanning two neighbouring RBDs and lock the spike in a closed conformation^{28–30} (BG10-19 and S2M11). Unexpectedly, S2L20-CVR, which recognizes an N-terminal domain (NTD) epitope (site iv), promoted robust entry, challenging the previous hypothesis that NTD-recognizing antibodies are insufficient to induce SARS-CoV-2 membrane fusion and entry in the absence of ACE2^{22,32} (Fig. 2c). We further demonstrated expression, antigen binding, pseudovirus entry and membrane fusion for selected CVRs (Fig. 2d).

To establish the molecular basis of functional CVR design, we hypothesized that CVR function depends on their ability to induce proper conformational changes that lead to downstream events required for membrane fusion, particularly RBD opening and exposure and cleavage of the S₂' cleavage site for fusion activation, as previously proposed for the S230 SARS-CoV-1 monoclonal antibody^{20,33,38}, (Fig. 2e). We found that only scFv-mouse IgG Fc (scFv-mFc) corresponding to functional CVRs induced the exposure of the 76E1 epitope

Article

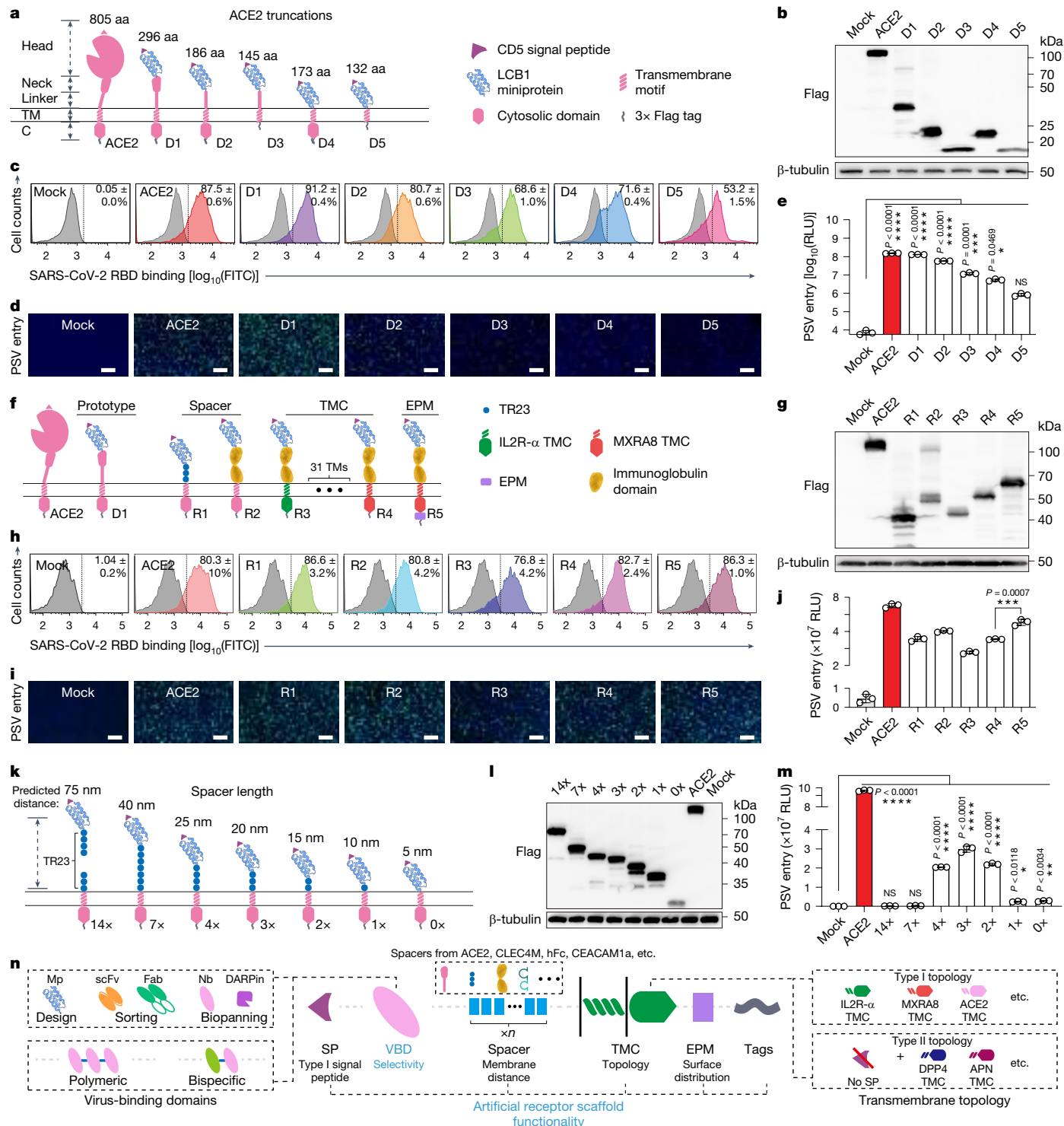


Fig. 1 | Modular design of CVRs for efficient coronavirus entry. **a–e**, Dissecting the importance of ACE2 sequences for its viral receptor function. **a**, Schematic representation illustrates the LCB1-ACE2 chimera with stepwise truncated ACE2 sequences. C, cytosolic domain; TM, transmembrane domain; aa, amino acids. **b,c**, Protein expression levels (**b**) and SARS-CoV-2 RBD-mouse IgG Fc (mFc) binding efficiency (**c**) in HEK293T cells transiently expressing the specified chimeras. **d,e**, SARS-CoV-2 pseudovirus (PSV) entry in HEK293T cells expressing each chimera was demonstrated by GFP imaging (**d**) and quantified (**e**). RLU, relative light units. Scale bars, 200 μ m. **f–j**, Function of chimeric receptors that have the remaining ACE2 sequences substituted by domains from other proteins. **f**, Schematic representation of CVRs carrying exogenous spacer, TMC and EPM sequences. **g–j**, CVR expression (**g**), SARS-CoV-2 spike RBD-mFc binding (**h**) and pseudovirus entry efficiency demonstrated by GFP imaging (**i**)

and quantification (**j**) in HEK293T cells transiently expressing the indicated chimeric receptors. Scale bars, 200 μ m. **k–m**, The effect of spacer length on CVR receptor function. **k**, Schematic representation illustrating CVRs with various TR23 tandem repeats, showing predicted spacer length. **l,m**, CVR expression (**l**) and SARS-CoV-2 pseudovirus entry efficiency (**m**) were evaluated in HEK293T cells transiently expressing the indicated CVRs. **n**, Schematic illustration of the modular design strategy for CVRs. Mp, miniprotein; Nb, nanobody. Data are representative of at least two independent transfections (**b,g,l**) and functional assays (**c–e,h–j,m**) with similar results. Data are mean \pm s.d. Experiments in **c–e,h–j,m** performed as biological triplicates; dashed lines in **c,h** denote thresholds for positive binding. One-way ANOVA followed by Dunnett's test (**e,j**); unpaired two-tailed Student's *t*-test (**m**). * $P < 0.05$, ** $P < 0.01$, *** $P < 0.001$, **** $P < 0.0001$; NS, not significant ($P > 0.05$).

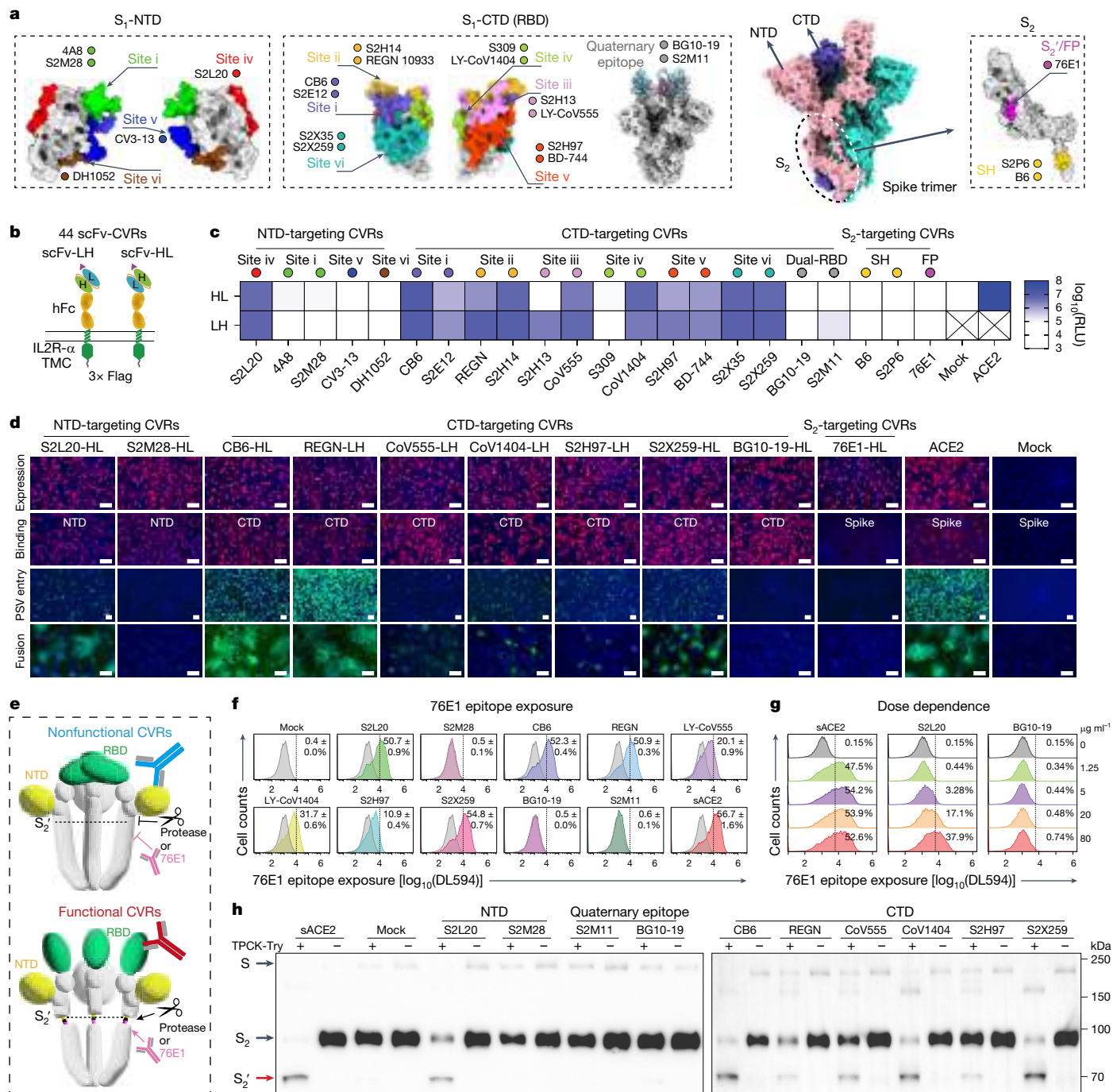


Fig. 2 | Effects of binding epitopes on receptor function. **a**, SARS-CoV-2 neutralizing epitopes of 22 neutralizing antibodies in spike NTD, CTD and S₂ subunits shown on the protein structure (Protein Data Bank (PDB) 6XR8). FP, fusion peptide; SH, stem helix. **b**, Schematic representation of 44 scFv-CVRs with N-terminal light chain or heavy chain. **c**, Heat map showing SARS-CoV-2 pseudovirus entry efficiency in HEK293T cells transiently expressing the indicated scFv-CVRs. Data are plotted as mean ($n = 3$ wells of independently infected cells), representative of two independent experiments with similar results. **d**, Demonstration of CVR expression, antigen binding, pseudovirus entry and spike-mediated cell–cell fusion in HEK293T cells expressing the indicated scFv-CVRs. Scale bars, 100 μ m. Images representative of two independent assays with similar results. **e**, Cartoon showing the functional receptor-mediated conformational change in the RBD, and subsequent

exposure of the 76E1 binding epitope and proteolytic cleavage at the S₂' cleavage site. **f**, Flow cytometry analysis of 76E1 epitope exposure in SARS-CoV-2 spike in the presence of indicated soluble scFv-mFc recombinant proteins. Data are mean \pm s.d. ($n = 3$ biological triplicates), representative of two independent experiments. **g**, Dose-dependent exposure of 76E1 epitope following coincubation with soluble hACE2 (sACE2) or S2L20 scFv-mFc, which was not detected with BG10-19 scFv-mFc. Data are representative of two independent experiments with similar results. **f,g**, Dashed lines denote thresholds for positive ratio calculation. **h**, Trypsin-mediated cleavage at the S₂' site in SARS-CoV-2 pseudovirus particles in the presence of 100 μ g ml⁻¹ of the indicated scFv-mFc. TPCK-trypsin (Try) was used at 10 μ g ml⁻¹. Blots are representative of at least four independent cleavage assays with similar results.

in a dose-dependent manner (Fig. 2e–g and Extended Data Fig. 6c), consistent with ACE2-induced exposure of the S₂' cleavage site and fusion peptide³⁶. Furthermore, increased protease accessibility to and

processing of the S₂' cleavage site induced by functional scFv-mFc align with data from 76E1 epitope exposure assays (Fig. 2h and Extended Data Fig. 6d).

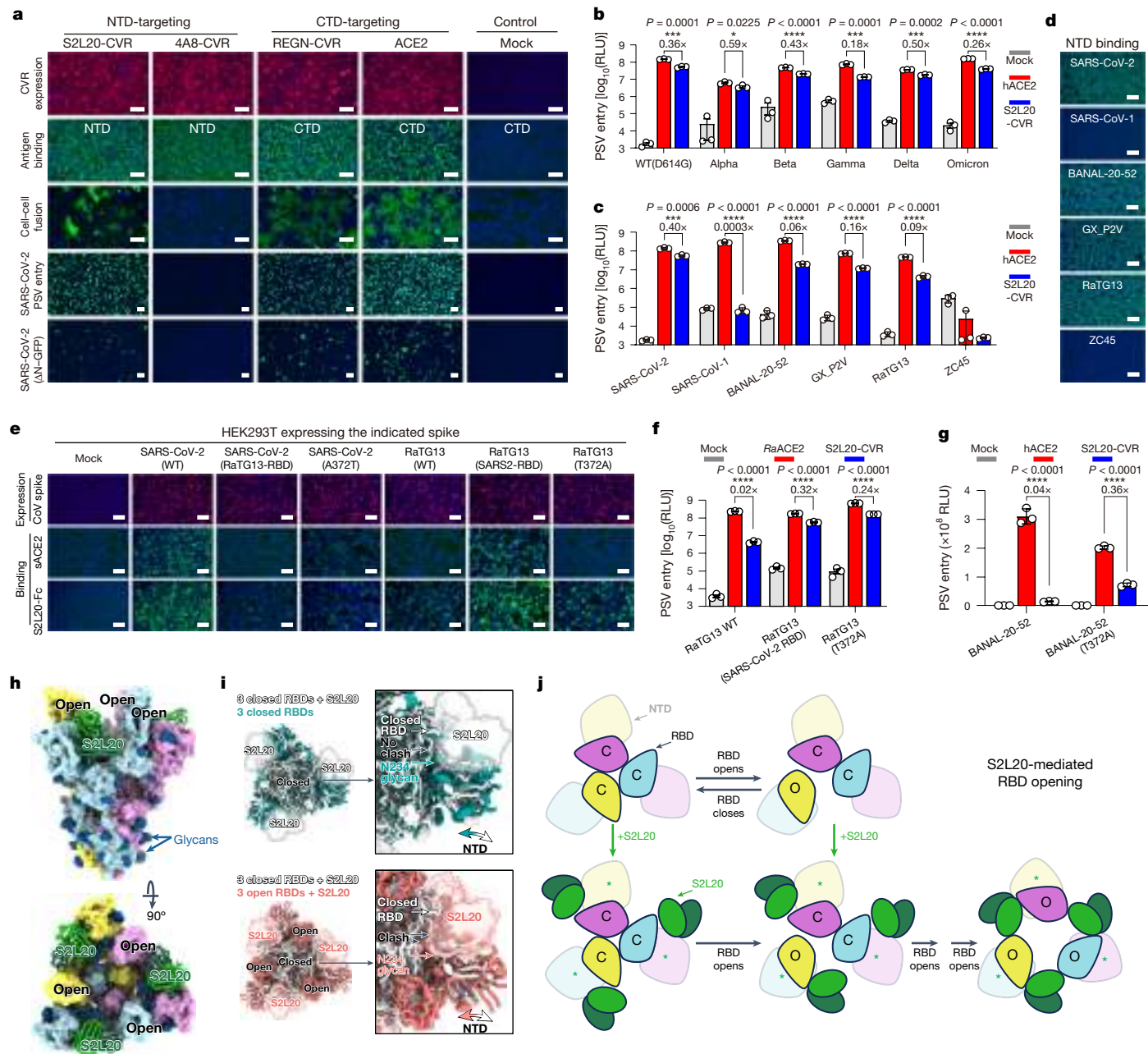


Fig. 3 | NTD-mediated sarbecovirus entry promoted by S2L20-CVR. **a**, CVR expression, SARS-CoV-2 spike NTD– or CTD–mFc binding, cell–cell fusion, pseudovirus entry and infection by SARS-CoV-2 with N protein substituted with GFP (SARS-CoV-2 Δ N-GFP) in HEK293T cells stably expressing the indicated CVRs. Data are representative of two independent transfection and functional assays. **b,c**, Pseudovirus entry of SARS-CoV-2 variants of concern (**b**) or different sarbecoviruses (**c**) in HEK293T cells stably expressing hACE2 or S2L20-CVR. **d**, Sarbecovirus spike NTD–mFc binding efficiencies in HEK293T cells expressing S2L20-CVR. Data are representative of three independent assays. **e**, Spike expression levels and corresponding soluble hACE2 (sACE2) or S2L20-mFc binding efficiencies. Data are representative of two independent binding assays. **f,g**, Effect of T372A mutation on S2L20-CVR-supported pseudovirus entry of RaTG13 (**f**) or BANAL-20-52 (**g**). *Ra*ACE2, *R. affinis* ACE2 allele 9479. **h**, Cryo-EM structure of SARS-CoV-2 Wuhan-Hu-1 Hexapro spike ectodomain trimer bound to the S2L20 Fab. Spike protomers are shown in pink, cyan, and

gold; N-linked glycans are dark blue; S2L20 Fab variable heavy and light chains are dark green and light green, respectively. **i**, Top, superimposition (based on the S₂ subunit) of the structures of S2L20-bound SARS-CoV-2 spike with RBDs in the closed confirmation (white; PDB 7N8H) and the apo structure with RBDs in the closed confirmation (teal; PDB 7K43). Bottom, superimposition (based on the S₂ subunit) of the structures of S2L20-bound SARS-CoV-2 spike with RBDs in the closed (white; 7N8H) and open (red; this study) conformations. Right, zoomed-in views of the interface between the NTD, RBD and S2L20. S2L20 is shown as a semi-transparent surface. The S2M11 Fab is not shown for clarity. **j**, Proposed mechanism of S2L20-mediated RBD opening and stabilization. C, closed state; O, open state. Asterisks indicate NTD repositioning. In **b,c,f,g**, data are mean \pm s.d. ($n = 3$ wells of independently infected cells) from two independent experiments. Ratios indicate pseudovirus entry supported by S2L20-CVR as a fraction of entry supported by ACE2. Unpaired two-tailed Student's *t*-tests. Scale bars, 100 μ m.

NTD-mediated entry by S2L20-CVR

We next sought to characterize NTD-mediated entry promoted by S2L20-CVR. We confirmed that S2L20-CVR acts as a functional receptor

for SARS-CoV-2, supporting membrane fusion, pseudovirus entry and authentic virus infection (Fig. 3a). Additionally, S2L20-CVR effectively facilitated pseudovirus entry of the five SARS-CoV-2 variants of concern that we tested and three other sarbecoviruses (BANAL-20-52, RaTG13

and GX_P2V) (Fig. 3b–d and Extended Data Fig. 7a). S2L20-CVR did not support entry of SARS-CoV-1 or ZC45 owing to lack of binding³² (Fig. 3c,d).

Despite showing similar NTD-binding efficiency, S2L20 supported entry of RaTG13 and BANAL-20-52 with lower efficiency than that of SARS-CoV-2 (Fig. 3c,d). Since the lack of an N370 glycan has been reported to be a distinct feature of SARS-CoV-2, we generated several mutants to investigate the effect of CTD sequences and of the N370 glycan on S2L20-CVR-mediated entry³⁹. A SARS-CoV-2 spike containing either the RaTG13 RBD or an A372T (glycan knock-in) substitution exhibited weaker binding to the soluble forms of hACE2 or S2L20-mFc than spike proteins with the SARS-CoV-2 RBD. We note that RaTG13 has a lower affinity for hACE2 than for an ACE2 orthologue from its host species (*Rhinolophus affinis*) (Fig. 3e). We hypothesized that the N370 glycan might sterically interfere with S2L20 binding owing to its proximity to the NTD-bound S2L20 Fab fragment. Consistently, the T372A mutation in the RaTG13 or BANAL-20-52 spike, which abolishes glycosylation at N370, significantly enhanced S2L20-CVR mediated entry⁴⁰ (Fig. 3f,g and Extended Data Fig. 7b–d).

We next investigated whether virus-neutralizing antibodies that target the SARS-CoV-2 spike CTD could interfere with NTD-mediated entry in cells expressing S2L20-CVR in comparison with hACE2-expressing cells. As expected, S2L20 exhibited higher neutralizing activity in cells expressing S2L20-CVR. Notably, although several antibodies (LY-CoV555, S309 and S2X259) showed reduced neutralizing efficiency in cells expressing S2L20-CVR, some CTD-binding antibodies exhibited similar neutralizing activity in both models (Extended Data Fig. 7e). These data suggest an association between the RBD and S2L20-CVR-mediated entry.

A prior study described the cryo-EM structure of S2L20 in complex with SARS-CoV-2 BA.5 spike, in which the three RBDs are in the up conformation, whereas the apo BA.5 spike structure has the three RBDs in the down conformation^{41,42}. By contrast, other NTD-targeting antibodies, including 4A8, CV3-13 and DH1052, do not appear to induce the RBD up conformation^{43–45} (Extended Data Fig. 7f). RBD opening can also be elicited by binding of ACE2, RBM-targeting antibodies and minibinders, or binding of any antibodies that target an RBD epitope that is occluded in the closed state^{24,38,46–49}. Therefore, we hypothesized that similar to ACE2, S2L20-CVR induces RBD opening, thereby promoting viral entry. To gain further insights into how this might occur, we obtained a cryo-EM structure of the S2L20 Fab bound to SARS-CoV-2 Wuhan-Hu-1 spike ectodomain with stabilizing HexaPro mutations (Fig. 3h, Extended Data Fig. 7g and Extended Data Table 1). Our structure features one S2L20 Fab bound to each of the three spike NTDs and three open RBDs instead of the previously described mixture of up and down RBD states for the apo spike⁵⁰ (Fig. 3h). However, we previously found that S2L20 can bind to the spike ectodomain when all the RBDs are locked closed, owing to the presence of the S2M11 Fab that recognizes a quaternary epitope spanning two neighbouring RBDs (Fig. 3i). Relative to closed S2L20-bound spike structures^{51,52}, the open S2L20-bound spike structure exhibits a repositioning of the NTDs and bound S2L20 along with stabilization of a conformation of the N234 glycan that would be sterically incompatible with subsequent RBD closing (Fig. 3i). Overall, these data support a molecular ratchet mechanism for S2L20-mediated RBD opening, whereby: (1) S2L20 can bind NTDs adjacent to closed RBDs, and when an RBD opens, the NTD and S2L20 shift to a position that blocks subsequent RBD closing; or (2) S2L20 could bind to NTDs adjacent to already open RBDs, thereby preventing them from adopting the closed state. Consistent with this hypothesis, incubation of purified spike ectodomain (without stabilizing proline substitutions) with S2L20 triggered fusogenic conformational changes in spike, resulting in post-fusion trimers (Fig. 3j and Extended Data Fig. 7h).

Although the induction of three RBDs in the up conformation upon S2L20 binding appears to be crucial for S2L20-CVR functionality,

CEACAM1a is an entry receptor for MHV despite recognizing an NTD surface proximal to the one targeted by the 4A8 SARS-CoV-2 antibody, which does not alter RBD opening or support viral entry^{5,43,53} (Extended Data Fig. 7i). This suggests that different coronaviruses might adopt distinct receptor recognition mechanisms to achieve NTD-mediated entry, or that yet undiscovered triggering mechanisms lead to MHV RBD opening and viral entry, as recently observed for HKU1^{12,54,55}.

CVR generalizability among coronaviruses

We extended our approach to generating CVRs for 12 coronaviruses from 6 subgenera, most of which have no known receptors¹ (Fig. 4a and Supplementary Table 1). To develop effective VBDs, we used magnetic beads and immunotube-assisted phage display biopanning to screen for coronavirus spike-specific nanobodies from naive libraries (Extended Data Fig. 8a). Lead CVR nanobodies were identified through validated binding to the RBD or S₁ subunit (Extended Data Fig. 8b and Supplementary Table 3). We also included Nb27, a broadly neutralizing nanobody that cross-reacts with RS HuB2019A and several other sarbecoviruses⁵⁶ (Extended Data Fig. 8c). We determined the binding kinetics of the selected nanobodies to the 12 coronavirus antigens through biolayer interferometry (BLI) assays (Extended Data Fig. 8d,e). We demonstrated efficient spike-mediated pseudovirus entry and cell–cell membrane fusion in cells stably expressing the indicated CVRs, achieving approximately 10²- to 10⁴-fold increases in pseudovirus entry compared with mock controls (Fig. 4b,c). CVRs with an EPM exhibited better cell surface localization and promoted more efficient entry (Extended Data Fig. 8f,g). The 2D1-CVR carrying an HKU1 RBD-targeting nanobody 2D1 exhibited similarly effective receptor function to TMPRSS2 (Extended Data Fig. 8h–k). Moreover, several CVRs designed for human coronavirus 229E and MHV-A59 supported efficient membrane fusion and authentic virus propagation, including 1B3-CVR, which targets the CTD of MHV spike (Fig. 4d–g).

We next evaluated the CVR-based infection models for neutralizing antibody assessment. We compared the neutralizing activity of sera collected from people who had recovered from COVID-19 or vaccinated individuals in HEK293T cells expressing ACE2, LCB1-CVR and Nb24-CVR²⁷. We observed similar overall serum inhibitory profiles between the three receptors, although slight differences were noted with Nb24-CVR, which recognizes an RBD epitope distant from the RBM (Extended Data Fig. 9a), possibly owing to modulation of apparent neutralization potencies resulting from distinct receptor usage or expression levels. This indicates the utility of the CVR-based system for evaluating the effectiveness of humoral immunity, ideally using CVRs that recognize the RBM region. We evaluated the cross-reactivity of several antibodies with broad neutralizing activity against a panel of coronaviruses, and found that 76E1 exhibits the greatest neutralization breadth, consistent with conservation of its epitope (Extended Data Fig. 9b,c). Furthermore, we investigated the potential of the CVR-based infection system for evaluating antiviral reagents targeting different entry steps, including proteolytic cleavage, endosome acidification and membrane fusion^{10,57–59}. We observed similar inhibitory efficacies when comparing spike-mediated entry via ACE2 and LCB1-CVR (Extended Data Fig. 9d). We further tested the effects of these inhibitors on SARS-CoV-2, HKU1, HKU3 and HKU5 entry in HEK293T cells expressing the corresponding CVRs. The overall efficiencies of entry inhibition were similar for SARS-CoV-2, HKU1 and HKU3, whereas HKU5 (HKU5-1, LMH03f isolate) exhibited a higher sensitivity to the TMPRSS2 inhibitor camostat than to the cathepsin inhibitor E64d (Extended Data Fig. 9e). The fusion inhibitor EK1C4⁵⁷, the optimized form of human coronavirus OC43 heptad repeat 2 (HR2) lipopeptide, exhibited a broad-spectrum inhibitory effect (Extended Data Fig. 9e).

To evaluate CVR support for multiple rounds of virus propagation, we created propagation-competent recombinant vesicular stomatitis viruses (pcVSVs) by replacing the VSV-G gene with HKU3 or HKU5 spike

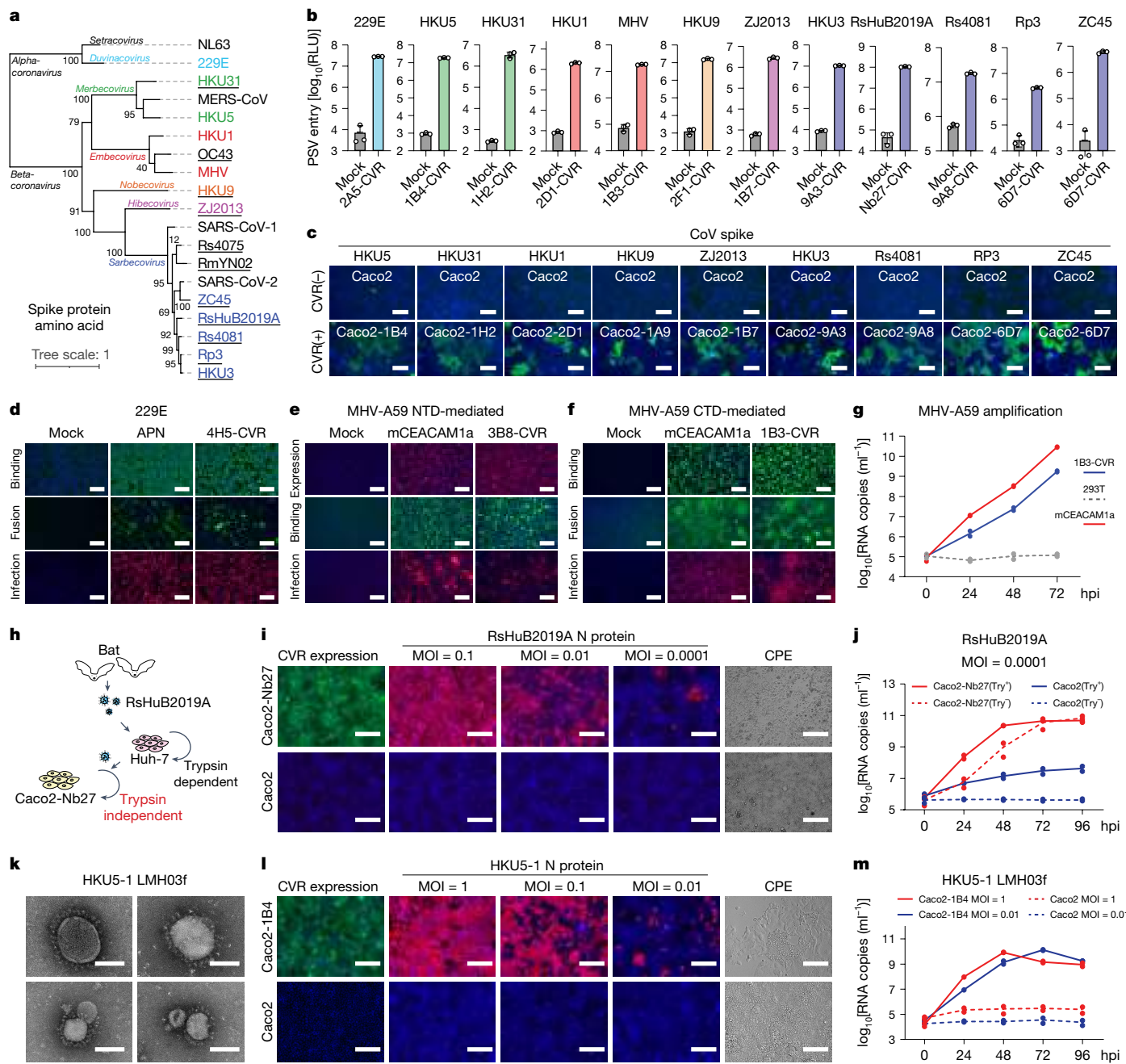


Fig. 4 | CVR-supported entry and amplification of various coronaviruses. **a**, Phylogenetic tree based on coronavirus spike amino acid sequences. Underlined species are those without known cellular receptors. **b**, Pseudovirus entry of twelve coronaviruses in HEK293T cells transiently expressing the indicated CVRs. Data are mean \pm s.d. (biological triplicates), representative of three independent infection assays. **c**, Cell-cell fusion promoted by indicated coronavirus spike in Caco2 cells with or without stable expression of indicated CVRs with trypsin treatment. Data are representative of three independent experiments. **d**, Coronavirus 229E S₁-mFc binding, cell-cell fusion and authentic 229E infection in HEK293T cells stably expressing aminopeptidase N (APN) or 4H5-CVR. **e,f**, MHV-A59 antigen binding, cell-cell fusion and authentic MHV infection in HEK293T cells stably expressing mouse CEACAM1a (mCEACAM1a) or NTD-targeting (e) or CTD-targeting (f) CVRs. **g**, MHV-A59 RNA copies in supernatant from infected cells expressing mCEACAM1a or 1B3-CVR. hpi, hours post-infection. **h**, Cartoon illustrating different trypsin dependence of viruses. Bat virus (RsHuB2019A) is trypsin-dependent, while Huh-7 and Caco2-Nb27 are trypsin-independent.

RSHuB2019A propagation in Huh-7 and Caco2-Nb27 cells. **i**, CVR expression, N protein and cytopathic effect (CPE) in cells inoculated with RSHuB2019A at the indicated MOI (no trypsin). **j**, Accumulation of viral RNA copies in supernatant of the indicated cells infected with RSHuB2019A. Try⁺, 100 μ g ml⁻¹ trypsin in DMEM + 2% FBS. **k**, Transmission electron microscopy analysis of HKU5-1 virions. Images are representative of a single experiment. **l**, CVR expression, N protein and cytopathic effect in the indicated cells inoculated with HKU5-1 at the indicated MOI. **m**, Accumulation of HKU5 RNA copies in supernatant of cells inoculated with HKU5-1 at the indicated MOI. Infection was detected by spike immunofluorescence (d-f) or N protein immunofluorescence (i,l) 24 hpi. In **g,j,m** data are the number of RNA copies from two independently infected wells of cells, with each point representing the mean of technical duplicates from quantitative PCR with reverse transcription (RT-qPCR). In **d-g,i,j,l,m**, data are from at least two independent experiments with similar results for each virus. Scale bars for **c-f**, 100 μ m; for **k,l**, 60 nm; for **i,l,m**, 125 μ m.

genes and additionally incorporating a GFP-expressing cassette for visualization (Extended Data Fig. 10a). pcVSV-HKU3 and pcVSV-HKU5 were successfully rescued with the aid of VSV-G provided in *trans*

(Extended Data Fig. 10b). We observed efficient spike-dependent propagation of pcVSV-HKU3 and pcVSV-HKU5 in CVR-expressing cells, as evidenced by syncytia formation with green fluorescence and viral

RNA accumulation, which was further enhanced by exogenous trypsin (Extended Data Fig. 10c–g). Subsequently, we investigated whether CVRs could promote the propagation of authentic coronaviruses that are difficult to culture. RsHuB2019A is an ACE2-independent bat *Sarbecovirus* that was recently isolated from field samples³. Isolation and propagation of this virus has been carried out in Huh-7 cells under serum-free culture conditions with exogenous trypsin, and viral infection is difficult to detect while maintaining normal cell morphology (Fig. 4h). We found that Caco2 cells expressing Nb27-CVR (Caco2-Nb27) efficiently supported RsHuB2019A propagation, even at very low multiplicity of infection (MOI) and in trypsin-free culture medium supplemented with 2% fetal bovine serum (FBS), enabling observation of cytopathic effect (Fig. 4i,j and Extended Data Fig. 10h,i).

We next explored the feasibility of rescuing or isolating authentic HKU5 using CVR-expressing cells. Utilizing a coronavirus reverse genetics approach, we generated a full-length infectious clone of wild-type HKU5 (HKU5-1, LMH03f isolate) with open reading frame 5 (ORF5) replaced by a sequence encoding a fluorescent protein reporter (ZsGreen-HiBiT (ZGH)) (Extended Data Fig. 10j). Using Caco2 cells expressing 1B4-CVR that generated by an HKU5-specific nanobody 1B4 (Caco2-1B4), we rescued both wild-type and ZGH-expressing versions of HKU5-1 authentic viruses and isolated another HKU5 strain (PaGD2014/15) from a bat anal swab sample (Fig. 4l,m and Extended Data Fig. 10k–n). Electron microscopy revealed a typical morphology of ‘crown’-shaped HKU5-1 virions (Fig. 4k). Efficient amplification was observed in cells inoculated with HKU5-1 at different MOIs, as indicated by nucleocapsid (N) protein immunostaining and the accumulation of viral RNA in the supernatant (Fig. 4l,m). Consistent with previous reports, HKU5 was weakly amplified in Vero E6 cells in the presence of exogenous trypsin^{60,61} (Extended Data Fig. 10o). We detected two mutations (T76R and K519T) in HKU5-1 spike after ten passages in Caco2-1B4 cells without any significantly altered biological features of trypsin dependence in infecting Caco2 cells (Extended Data Fig. 10p,q). Finally, we assessed the activities of several antiviral reagents against HKU5-1 infection in Caco2-1B4 cells. Consistent with the pseudovirus entry assay data (Extended Data Fig. 9e), most of the tested antiviral reagents blocked HKU5-1 infection, especially EK1⁵⁹ and EK1C4 peptides (Extended Data Fig. 10r–t). However, HKU5-1 infection was inhibited by camostat but not by E64d, in line with its sequence features at the typical protease cleavage sites⁶⁰ (Extended Data Fig. 10r,t,u).

Discussion

The COVID-19 pandemic has emphasized the immediate need for research on zoonotic risks of animal coronaviruses to prepare for future outbreaks. However, in-depth research and vaccine and anti-viral compound development are impeded by the lack of knowledge about the receptors used by many viruses and our resulting inability to isolate and culture these viruses¹. Here we introduce a technique for engineering functional viral receptors for various coronaviruses, which involves the modular design of ARSs for functionality and the customization of viral binding domains (VBDs) for selectivity (Extended Data Fig. 11). Theoretically, receptors can be designed for most naturally existing viruses if both ARSs and VBDs are optimized, although requirements and challenges for achieving optimal receptor function may vary among viruses. We demonstrate that single polypeptide chain structures such as nanobodies or scFVs are preferable modules for VBD design compared with Fab fragments. We also highlight the potential of computational de novo design of VBDs. In addition to efficient binding to viral surface proteins, an optimal distance between the VBD and the cell membrane is crucial for CVR functionality, although this distance may vary for spacers with distinct structures, orientations and flexibility. Additionally, we also show the potential of the soluble adapter strategy to support viral entry, achieved using a bispecific adapter that retargets virus to receptors on the cell surface.

The ability of specific coronavirus spike surfaces to function as receptor-binding motifs may depend on whether a VBD bound to this region can induce the necessary conformational changes that lead to the activation of the fusion machinery. Therefore, CVRs targeting the S₂ subunit, most NTD epitopes, and some CTD epitopes are nonfunctional. We found a strong link between the receptor function of CVRs and their ability to expose the 76E1 epitope, which encompasses the S_{2'} cleavage site. This aligns with the allosteric conformational changes induced in spike by the endogenous receptor that lead to coronavirus entry^{36,38,62}. However, the specific conformational changes required to expose this epitope remain unclear, although a transition of the RBD from the down to the up conformation appears to be crucial⁹. Consistently, CVRs that recognize epitopes that are only present in the closed spike trimer with the three RBDs in the down conformation (locking the spike shut), did not support entry^{29,30}.

We demonstrate that coronaviruses can utilize both NTD and CTD of spike for receptor engagement, as exemplified by the NTD-targeting S2L20-CVR, as long as the previously mentioned requirements are fulfilled. Additionally, we show that MHV infection can be promoted by NTD-targeting or CTD-targeting CVRs, suggesting the possibility that MHV or related viruses may recognize alternative receptors through the CTD. It is also possible that other coronaviruses rely on (or could evolve to use) NTD-mediated entry. Notably, two infection-enhancing antibodies that target the SARS-CoV-2 spike NTD—CV3-13 and DH1052 (ref. 44)—did not yield functional CVRs, highlighting differences in mechanisms between antibody-dependent enhancement (ADE) of viral entry mediated by soluble antibodies and viral entry mediated by membrane-anchored CVRs in vitro. Our study has meaningful implications for understanding ADE, particularly for the Fc_YR receptor-mediated mechanism that can be detected both in vitro and in vivo^{21–23}. However, the efficiency of Fc_YR receptor-mediated entry is probably limited by multiple factors, such as suboptimal membrane distance, suboptimal antibody concentration, neutralization effects and the usually nonproductive viral infection in cells that endogenously express Fc_YR²³. This study also brings attention to the possibility of viral entry promoted by membrane-anchored antibodies such as B cell receptors, but this phenomenon and its consequences remain to be investigated in vivo. Currently, there is no substantial evidence of ADE restricting antibody therapy and vaccination against SARS-CoV-2. A rare case of ADE with negative outcomes in real-life situations occurs with feline infectious peritonitis virus, which targets macrophages⁶³.

The CVR strategy enables the manipulation of cell susceptibility to various viruses, thereby facilitating the isolation or rescue of viruses regardless of native receptor usage or cell tropism (Extended Data Fig. 11). Overcoming limitations of native receptors underscores the potential of this strategy, such as enhancing affinity, altering epitopes, adjusting specificity, changing structures or removing physiological functional interference and cell-type restrictions. CVR-based infection models can be utilized as alternative tools for assessing antibodies or other antiviral reagents against viruses whose cellular receptors remain unidentified, thereby supporting pandemic preparedness. However, several limitations should be noted when employing CVR-based models. Differences in targeted epitopes and interaction modes may result in inconsistencies when evaluating neutralizing antibodies or vaccines. Furthermore, differences may exist in the entry pathway for some CVRs compared with native receptors. Notably, CVR transgenic mice could be useful for evaluating viral pathogenesis and vaccine or antiviral protection in vivo. However, variations in tissue expression patterns may limit how closely this allows us to recapitulate natural infection, as with K18-hACE2 mice.

This study presents a novel method for rescuing, isolating and culturing coronaviruses based on genetically modified cell culture models independent of native receptors. Our findings provide a foundation for the design of viral infection models for difficult-to-culture coronaviruses and other viruses, and will facilitate further advances in basic

research on various infectious diseases and accelerate the rapid development of countermeasures for the benefit of public health worldwide.

Online content

Any methods, additional references, Nature Portfolio reporting summaries, source data, extended data, supplementary information, acknowledgements, peer review information; details of author contributions and competing interests; and statements of data and code availability are available at <https://doi.org/10.1038/s41586-024-08121-5>.

1. Millet, J. K., Jaimes, J. A. & Whittaker, G. R. Molecular diversity of coronavirus host cell entry receptors. *FEMS Microbiol. Rev.* **45**, fuaa057 (2021).
2. Li, F. Receptor recognition mechanisms of coronaviruses: a decade of structural studies. *J. Virol.* **89**, 1954–1964 (2015).
3. Guo, H. et al. Isolation of ACE2-dependent and -independent sarbecoviruses from Chinese horseshoe bats. *J. Virol.* **97**, e0039523 (2023).
4. Cui, J., Li, F. & Shi, Z.-L. Origin and evolution of pathogenic coronaviruses. *Nat. Rev. Microbiol.* **17**, 181–192 (2019).
5. Walls, A. C. et al. Cryo-electron microscopy structure of a coronavirus spike glycoprotein trimer. *Nature* **531**, 114–117 (2016).
6. Walls, A. C. et al. Tectonic conformational changes of a coronavirus spike glycoprotein promote membrane fusion. *Proc. Natl Acad. Sci. USA* **114**, 11157–11162 (2017).
7. Walls, A. C. et al. Structure, function, and antigenicity of the SARS-CoV-2 spike glycoprotein. *Cell* **181**, 281–292.e6 (2020).
8. Peng, G. et al. Crystal structure of mouse coronavirus receptor-binding domain complexed with its murine receptor. *Proc. Natl Acad. Sci. USA* **108**, 10696–10701 (2011).
9. Yan, R. et al. Structural basis for the different states of the spike protein of SARS-CoV-2 in complex with ACE2. *Cell Res.* **31**, 717–719 (2021).
10. Hoffmann, M. et al. SARS-CoV-2 cell entry depends on ACE2 and TMPRSS2 and is blocked by a clinically proven protease inhibitor. *Cell* **181**, 271–280.e8 (2020).
11. Saunders, N. et al. TMPRSS2 is a functional receptor for human coronavirus HKU1. *Nature* **624**, 207–214 (2023).
12. McCallum, M. et al. Human coronavirus HKU1 recognition of the TMPRSS2 host receptor. *Cell* **187**, 4231–4245.e13 (2024).
13. Xiong, Q. et al. Close relatives of MERS-CoV in bats use ACE2 as their functional receptors. *Nature* **612**, 748–757 (2022).
14. Hofmann, H. et al. Human coronavirus NL63 employs the severe acute respiratory syndrome coronavirus receptor for cellular entry. *Proc. Natl Acad. Sci. USA* **102**, 7988–7993 (2005).
15. Starr, T. N. et al. ACE2 binding is an ancestral and evolvable trait of sarbecoviruses. *Nature* **603**, 913–918 (2022).
16. Lee, J. et al. Broad receptor tropism and immunogenicity of a clade 3 sarbecovirus. *Cell Host Microbe* **31**, 1961–1973.e11 (2023).
17. Lim, S., Zhang, M. & Chang, T. L. ACE2-independent alternative receptors for SARS-CoV-2. *Viruses* **14**, 2535 (2022).
18. Baggen, J. et al. TMEM106B is a receptor mediating ACE2-independent SARS-CoV-2 cell entry. *Cell* **186**, 3427–3442.e22 (2023).
19. Verheijen, M. H. et al. Redirecting coronavirus to a nonnative receptor through a virus-encoded targeting adapter. *J. Virol.* **80**, 1250–1260 (2006).
20. Wan, Y. et al. Molecular mechanism for antibody-dependent enhancement of coronavirus entry. *J. Virol.* **94**, e02015–19 (2020).
21. Maemura, T. et al. Antibody-dependent enhancement of SARS-CoV-2 infection is mediated by the IgG receptors FcYRIIA and FcYRIIIA but does not contribute to aberrant cytokine production by macrophages. *mBio* **12**, e0198721 (2021).
22. Kibria, M. G. et al. Antibody-mediated SARS-CoV-2 entry in cultured cells. *EMBO Rep.* **24**, e57724 (2023).
23. Junqueira, C. et al. FcYR-mediated SARS-CoV-2 infection of monocytes activates inflammation. *Nature* **606**, 576–584 (2022).
24. Cao, L. et al. De novo design of picomolar SARS-CoV-2 miniprotein inhibitors. *Science* **370**, 426–431 (2020).
25. Hoffmann, M. A. G. et al. ESCRT recruitment to SARS-CoV-2 spike induces virus-like particles that improve mRNA vaccines. *Cell* **186**, 2380–2391.e9 (2023).
26. Ying, T., Feng, Y., Wang, Y., Chen, W. & Dimitrov, D. S. Monomeric IgG1 Fc molecules displaying unique Fc receptor interactions that are exploitable to treat inflammation-mediated diseases. *MAbs* **6**, 1201–1210 (2014).
27. Xiang, Y. et al. Versatile and multivalent nanobodies efficiently neutralize SARS-CoV-2. *Science* **370**, 1479–1484 (2020).
28. Pinto, D. et al. Cross-neutralization of SARS-CoV-2 by a human monoclonal SARS-CoV antibody. *Nature* **583**, 290–295 (2020).
29. Scheid, J. F. et al. B cell genomics behind cross-neutralization of SARS-CoV-2 variants and SARS-CoV. *Cell* **184**, 3205–3221.e24 (2021).
30. Tortorici, M. A. et al. Ultrapotent human antibodies protect against SARS-CoV-2 challenge via multiple mechanisms. *Science* **370**, 950–957 (2020).
31. Cui, Z. et al. Structural and functional characterizations of infectivity and immune evasion of SARS-CoV-2 Omicron. *Cell* **185**, 860–871.e13 (2022).
32. McCallum, M. et al. N-terminal domain antigenic mapping reveals a site of vulnerability for SARS-CoV-2. *Cell* **184**, 2332–2347.e16 (2021).
33. Sun, X. et al. Neutralization mechanism of a human antibody with pan-coronavirus reactivity including SARS-CoV-2. *Nat Microbiol* **7**, 1063–1074 (2022).
34. Pinto, D. et al. Broad betacoronavirus neutralization by a stem helix-specific human antibody. *Science* **373**, 1109–1116 (2021).
35. Sauer, M. M. et al. Structural basis for broad coronavirus neutralization. *Nat. Struct. Mol. Biol.* **28**, 478–486 (2021).
36. Low, J. S. et al. ACE2-binding exposes the SARS-CoV-2 fusion peptide to broadly neutralizing coronavirus antibodies. *Science* **377**, 735–742 (2022).
37. Piccoli, L. et al. Mapping neutralizing and immunodominant sites on the SARS-CoV-2 spike receptor-binding domain by structure-guided high-resolution serology. *Cell* **183**, 1024–1042.e21 (2020).
38. Walls, A. C. et al. Unexpected receptor functional mimicry elucidates activation of coronavirus fusion. *Cell* **176**, 1026–1039.e15 (2019).
39. Zhang, S. et al. Loss of spike N370 glycosylation as an important evolutionary event for the enhanced infectivity of SARS-CoV-2. *Cell Res.* **32**, 315–318 (2022).
40. Ou, X. et al. Host susceptibility and structural and immunological insight of S proteins of two SARS-CoV-2 closely related bat coronaviruses. *Cell Discov* **9**, 78 (2023).
41. Chi, X. et al. Comprehensive structural analysis reveals broad-spectrum neutralizing antibodies against SARS-CoV-2 Omicron variants. *Cell Discov* **9**, 37 (2023).
42. Cao, Y. et al. BA.2.121, BA.4 and BA.5 escape antibodies elicited by Omicron infection. *Nature* **608**, 593–602 (2022).
43. Chi, X. et al. A neutralizing human antibody binds to the N-terminal domain of the Spike protein of SARS-CoV-2. *Science* **369**, 650–655 (2020).
44. Li, D. et al. In vitro and in vivo functions of SARS-CoV-2 infection-enhancing and neutralizing antibodies. *Cell* **184**, 4203–4219.e32 (2021).
45. Beaudoin-Bussières, G. et al. An Fc-enhanced NTD-binding non-neutralizing antibody delays virus spread and synergizes with a nAb to protect mice from lethal SARS-CoV-2 infection. *Cell Rep.* **38**, 110368 (2022).
46. Barnes, C. O. et al. Structures of human antibodies bound to SARS-CoV-2 spike reveal common epitopes and recurrent features of antibodies. *Cell* **182**, 828–842.e16 (2020).
47. Benton, D. J. et al. Receptor binding and priming of the spike protein of SARS-CoV-2 for membrane fusion. *Nature* **588**, 327–330 (2020).
48. Starr, T. N. et al. SARS-CoV-2 RBD antibodies that maximize breadth and resistance to escape. *Nature* **597**, 97–102 (2021).
49. Hunt, A. C. et al. Multivalent designed proteins neutralize SARS-CoV-2 variants of concern and confer protection against infection in mice. *Sci. Transl. Med.* **14**, eabn1252 (2022).
50. Hsieh, C.-L. et al. Structure-based design of prefusion-stabilized SARS-CoV-2 spikes. *Science* **369**, 1501–1505 (2020).
51. McCallum, M. et al. Molecular basis of immune evasion by the Delta and Kappa SARS-CoV-2 variants. *Science* **374**, 1621–1626 (2021).
52. McCallum, M. et al. SARS-CoV-2 immune evasion by the B.1.427/B.1.429 variant of concern. *Science* **373**, 648–654 (2021).
53. Shang, J. et al. Structure of mouse coronavirus spike protein complexed with receptor reveals mechanism for viral entry. *PLoS Pathog.* **16**, e1008392 (2020).
54. Wang, H. et al. TMPRSS2 and glycan receptors synergistically facilitate coronavirus entry. *Cell* **187**, 4261–4271.e17 (2024).
55. Pronker, M. F. et al. Sialoglycan binding triggers spike opening in a human coronavirus. *Nature* **624**, 201–206 (2023).
56. Xu, J. et al. Nanobodies from camelid mice and llamas neutralize SARS-CoV-2 variants. *Nature* **595**, 278–282 (2021).
57. Xia, S. et al. Inhibition of SARS-CoV-2 (previously 2019-nCoV) infection by a highly potent pan-coronavirus fusion inhibitor targeting its spike protein that harbors a high capacity to mediate membrane fusion. *Cell Res.* **30**, 343–355 (2020).
58. Xia, S. et al. Structural and functional basis for pan-CoV fusion inhibitors against SARS-CoV-2 and its variants with preclinical evaluation. *Signal Transduct. Target. Ther.* **6**, 288 (2021).
59. Xia, S. et al. A pan-coronavirus fusion inhibitor targeting the HR1 domain of human coronavirus spike. *Sci. Adv.* **5**, eaav4580 (2019).
60. Menachery, V. D. et al. Trypsin treatment unlocks barrier for zoonotic bat coronavirus infection. *J. Virol.* **94**, e01774–19 (2020).
61. Catanzaro, N. J. et al. ACE2 from Pipistrellus abramus bats is a receptor for HKU5 coronaviruses. Preprint at *bioRxiv* <https://doi.org/10.1101/2024.03.13.584892> (2024).
62. Qing, E. et al. Inter-domain communication in SARS-CoV-2 spike proteins controls protease-triggered cell entry. *Cell Rep.* **39**, 110786 (2022).
63. Takano, T., Kawakami, C., Yamada, S., Satoh, R. & Hohdatsu, T. Antibody-dependent enhancement occurs upon re-infection with the identical serotype virus in feline infectious peritonitis virus infection. *J. Vet. Med. Sci.* **70**, 1315–1321 (2008).

Publisher's note Springer Nature remains neutral with regard to jurisdictional claims in published maps and institutional affiliations.

Springer Nature or its licensor (e.g. a society or other partner) holds exclusive rights to this article under a publishing agreement with the author(s) or other rightsholder(s); author self-archiving of the accepted manuscript version of this article is solely governed by the terms of such publishing agreement and applicable law.

© The Author(s), under exclusive licence to Springer Nature Limited 2024

Methods

Cell lines

HEK293T (CRL-3216), VeroE6 (CRL-1586), A549 (CCL-185), BHK-21 (CCL-10), Caco2 (HTB-37), Neuro2a (CCL-131) and Tb 1 Lu (CCL-88) cells were purchased from the American Type Culture Collection (ATCC). Huh-7 cells (SCSP-526) were obtained from the Cell Bank of Type Culture Collection, Chinese Academy of Sciences. All cells were maintained in Dulbecco's Modified Eagle Medium (DMEM, Monad), supplemented with 10% FBS and with or without 1× penicillin G (100 U ml⁻¹)/streptomycin (100 µg ml⁻¹) (pen/strep). An II-hybridoma cell line (CRL-2700) producing a neutralizing mouse monoclonal antibody against VSV-G, was cultured in minimum essential medium with Earle's balanced salts solution, 2 mM L-glutamine (Gibco) and 5% FBS. All cell lines were incubated at 37 °C in 5% CO₂ with regular passage every 2–3 days.

Virus and host gene sequences

All viral genome or gene sequences were sourced from GenBank or GISAID databases with the following accession numbers. Viruses: SARS-CoV-1 (NC_004718), SARS-CoV-2 (NC_045512), MERS-CoV (NC_019843), HKU3 (DQ022305), Rp3 (DQ071615), HKU5-1 LMH03F (NC_009020), HKU31 (MK907286), HKU9 (NC_009021), Zhejiang2013 (NC_025217), Rs4081 (KY417143), MHV-A59 (NC_048217), NL63 (JX504050), 229E (OQ920101), HKU1 (NC_006577), OC43 (AY391777), RmYN02 (EPI_ISL_412977), ZC45 (MG772933), RsHuB2019A (OQ503498), GX_P2V (MW532698.1) and BANAL-20-52 (MZ937000.1). The spike protein for Rs4075 (KC880993), B.1.1.7/α (EPI-ISL-601443), B.1.351/β (EPI_ISL_678597), P.1/γ (EPI_ISL_906075), B.1.617.2/δ (EPI_ISL_2378732) and BA.2 (EPI_ISL_7580387). Receptors: human ACE2 (NM_001371415), *R. affinis* ACE2 (MT394208), DPP4 (NM_001935), APN (NM_001150), mCEACAM1a (NM_001039186), AXL (NM_001699), NRP1 (NM_001024628), SCARB1 (BC143319), KREMEN1 (NM_032045), ASGR1 (NM_001671), CD147 (AB085790), CLEC4M (KJ902090), LRRC15 (NM_001135057)⁶⁴, TMEM106B (NM_018374)¹⁸ and TMPRSS2 (NM_001135099). All receptor and viral gene sequences used in this study were commercially synthesized by Genewiz or GenScript. Supplementary Table 1 summarizes detailed information on these genes.

Plasmids

All plasmids expressing type I transmembrane CVRs were constructed by inserting the human codon-optimized CVR sequences into a lentiviral transfer vector (pLVX-EF1a-Puro, Genewiz) with an N-terminal CD5 leading sequence (MPMGLQPLATLYLLGMLVASVL) and C-terminal 3× Flag tag (DYKDHD-G-DYKDHD-IDYKDDDK). Type II transmembrane CVRs were constructed by replacing the C-terminal ectodomains with corresponding CVR modules, along with an N-terminal 3× Flag tag. Chimeric protein-coding sequences were generated using overlapping PCR, direct sequence synthesis, homologous recombination (Hieff Clone, YEASEN, 10922ES20), or restriction endonuclease digestion and ligation. All modules were connected with two or four amino acids (commonly G, S or T) that were encoded by one or two restriction endonuclease sites. The sequences of CVRs for illustrating the modular design strategy are summarized in Supplementary Table 2.

Plasmids expressing the spike glycoproteins from various coronaviruses for VSV pseudotyping were constructed by inserting human codon-optimized spike coding sequences into either the pCAGGS or pcDNA3.1(-) vectors with C-terminal 13–18 residues substituted with an HA tag (YPYDVVPDYA) to enhance VSV pseudotyping efficiency and facilitate detection⁶⁵. Several spike genes were also introduced into the pLVX-IRES-ZsGreen vectors for flow cytometry-related assays, including scFv-mFc binding and 76E1 epitope exposure assays.

Plasmids expressing secreted fusion proteins, including the coronavirus antigens, scFvs and nanobodies fused with human or mouse Fc, were constructed by inserting the coding sequences into pCAGGS. These constructs featured an N-terminal CD5 secretion leading sequence

(MPMGLQPLATLYLLGMLVASVL) and a C-terminal Twin-Strep Tag II following 3× Flag tandem sequences (WSHPQFEKGGGGGGSGGSWAWS HPQFEKGGGRSDYKDHDGDYKDHDIDYKDDDDK) for purification or detection. Plasmids encoding codon-optimized anti-ACE2 antibodies h1B11⁶⁶, or SARS-CoV-2 spike-targeting neutralizing antibodies B6, S2P6, 76E1, S2H97, S2L20, and REGN10933, LY-CoV555, S309, S2X259, S2M11 and BG10-19 were constructed by integrating the heavy-chain and light-chain coding sequences into pCAGGS with an N-terminal CD5 leader sequences, respectively. For split protein-based cell–cell fusion assays, the split protein genes were inserted into pLVX-EF1a-Puro. The coding sequences for the dual reporter split proteins, namely *Renilla* luciferase (RLuc) (residues 1–155)–sfGFP (residues 1–157) and sfGFP (residues 158–231)–RLuc (residues 156–311), are previously described¹³.

Stable cell lines

Cells stably expressing distinct CVRs and other receptors were established using lentivirus transduction and subsequent antibiotic selection. Lentiviruses carrying the target genes were generated by co-transfected lentiviral transfer plasmid (pLVX-EF1a-Puro) with packaging plasmids pMD2G (Addgene, 12259) and psPAX2 (Addgene, 12260) into HEK293T cells through GeneTwin (Biomed, TG101). The lentivirus-containing supernatant was pooled at 24 and 48 hours post-transfection (hpt). Cell transduction was performed in the presence of 8 µg ml⁻¹ Polybrene. Stable cell lines were selected and maintained in a growth medium supplemented with puromycin (1 µg ml⁻¹). Typically, cells that remained stable for at least ten days were used in subsequent experiments.

SARS-CoV-2 reactive polyclonal sera

SARS-CoV-2 polyclonal sera were obtained from vaccinated individuals (SARS-CoV-2 CoronaVac, Sinovac), approximately 21 days post-vaccination and people who had recovered from Wuhan COVID-19 infection (convalescent individuals) around one year post-infection, respectively. Ethical approval for the vaccinated individuals was granted by the Ethics Committee (seal) of Beijing Youan Hospital, Capital Medical University, with approval number LL-2021-042-K. The collection of sera from Wuhan COVID-19 convalescent individuals was conducted in collaboration with the Hubei Provincial Center for Disease Control and Prevention and Hubei Provincial Academy of Preventive Medicine (HBCDC), following written consent and under the approval of the Institutional Review Boards with the identification number 2021-012-01. Sera were heat-inactivated at 56 °C for 30 min.

Recombinant protein expression and purification

Proteins for binding, neutralizing or biopanning-related assays were produced in HEK293T by transient transfection with plasmids using GeneTwin reagent (Biomed, TG101-01), following the manufacturer's guidelines. Protein-containing supernatants were collected every 2–3 days post-transfection, pooled, clarified and subsequently purified. Proteins fused with Fc were captured using Pierce Protein A/G Plus Agarose (Thermo Scientific, 20424), eluted with pH 3.0 glycine (100 mM in H₂O), and immediately pH balanced by 1/10 volume of UltraPure 1 M Tris-HCl, pH 8.0 (Thermo Fisher Scientific, 15568025). Proteins with Twin-Strep Tag II (strep) were enriched using Strep-Tactin XT 4Flow high-capacity resin (IBA, 2-5030-002), washed, and eluted with buffer BXT (100 mM Tris/HCl, pH 8.0, 150 mM NaCl, 1 mM EDTA, 50 mM biotin). The eluted proteins were concentrated and buffer-exchanged to PBS through ultrafiltration, aliquoted and stored at –80 °C. Protein concentrations were determined using the Omni-Easy Instant BCA Protein Assay Kit (Epizyme, ZJ102).

Western blot

For detecting the cellular expression of CVRs or other receptors, cells were washed with PBS and lysed using RIPA buffer (50 mM Tris·pH 7.4, 150 mM NaCl, 1% Triton X-100, 0.5% sodium deoxycholate, 0.1%

Article

SDS, 25 mM β -glycerophosphate, 1 mM EDTA, and 1 mM PMSF) on ice for 15 min. The lysate was clarified by centrifugation at 12,000g at 4 °C for 15 min. The supernatant was combined with a 1:5 (v/v) ratio of 5× SDS loading buffer and incubated at 95 °C for 10 min. For detecting the spike packaging efficiency, the pseudovirus-containing supernatant was concentrated with a 30% sucrose cushion (30% sucrose, 15 mM Tris-HCl, 100 mM NaCl, 0.5 mM EDTA) at 20,000g for 1.5 h at 4 °C. The concentrated virus pellet was resuspended in 1× SDS loading buffer and incubated at 95 °C for 30 min. For detecting the S₂' cleavage of pseudovirus, the concentrated viruses were resuspended in DMEM in the presence of indicated concentrations of scFv-mFc or soluble ACE2 for 2 h at 4 °C, and then treated with 10 μ g ml⁻¹ TPCK-trypsin (Sigma-Aldrich, T8820) for 30 min at 37 °C, followed by mixing with a 1:5 (v/v) ratio 5× SDS loading buffer and incubated at 95 °C for 10 min.

After SDS-PAGE electrophoresis and PVDF membrane transfer, blots were blocked with 5% milk in PBS containing 0.1% Tween-20 (PBST) at room temperature for 1 h. Primary antibodies targeting Flag tag (Sigma-Aldrich, F1804, 1:10,000), HA (MBL, M180-3, 1:5,000), VSV-M (23H12) (Kerafast, EB0011, 1:10,000), β -tubulin (Immunoway, YM3030, 1:10,000) and GAPDH (AntGene, ANT325, 1:10,000) were diluted in PBST with 1% milk and incubated with the blot overnight at 4 °C. The stem helix-targeting monoclonal antibody S2P6 for coronavirus spike detection was used at 1 μ g ml⁻¹. After three washes with PBST, the blots were incubated with horseradish peroxidase-conjugated secondary goat antibodies against human (Sigma-Aldrich, A0170), rabbit (Sino Biological, SSA003), or mouse (Jackson Lab, 15-035-003) IgG (1:5,000). After extensive wash, blots were visualized using the LI-COR Odyssey CLx or the Omni-ECL Femto Light Chemiluminescence Kit (EpiZyme, SQ201) and a ChemiDoc MP Imaging System (Bio-Rad). Image Lab (version 5.2.1) was utilized to analyse western blot data. Uncropped and unprocessed full scans of gel source data are provided in Supplementary Figs. 1 and 2.

Live-cell binding assays

For detecting coronavirus antigens binding to cell surface expressed CVRs, NTD, CTD or S₁-Fc fusion proteins were diluted in DMEM and incubated with cells at 1 to 4 μ g ml⁻¹ for 1 h at 37 °C. Cells were washed twice with Hanks' Balanced Salt solution (HBSS) and incubated with 2 μ g ml⁻¹ Alexa Fluor 594- or Alexa Fluor 488-conjugated goat anti-mouse IgG (Thermo Fisher Scientific; A32742/A32723) for visualization. For detecting the Twin-Strep Tag II-labelled spike trimer or sACE2 binding, the incubated cells were treated with 1 μ g ml⁻¹ anti-Twin-Strep Tag II monoclonal antibody (Abbkine; ABT2230) for 30 min at 4 °C, washed twice with HBSS, and then subjected to fluorescence-labelled secondary antibody incubation. Finally, cells were incubated with Hoechst 33342 (1:5,000 in HBSS) for nuclear staining before imaging using a fluorescence microscope (Mshot, MI52-N).

Immunofluorescence for detecting receptor expression

Immunofluorescence assays were performed to assess the expression of the CVRs or other receptors carrying the C-terminal 3× Flag tags. In general, cells expressing the proteins were fixed with 100% methanol at room temperature for 10 min, washed once with PBS, and incubated with a mouse monoclonal antibody M2 specific to the Flag tag (Sigma-Aldrich, F1804, 1:1000) in 1% BSA/PBS at 37 °C for 1 h. After another wash with PBS, cells were incubated with 2 μ g ml⁻¹ Alexa Fluor 594-conjugated goat anti-mouse IgG (Thermo Fisher Scientific, A32742) diluted in 1% BSA/PBS for 1 h at 37 °C. Nuclei were stained with Hoechst 33342 (1:5,000 dilution in PBS). Images were captured and merged using a fluorescence microscope (Mshot, MI52-N).

Biolayer interferometry

Protein binding kinetics were evaluated through BLI assays conducted on the Octet RED96 instrument (Molecular Devices) at 25 °C, and shaking at 1,000 rpm. In brief, 20 μ g ml⁻¹ of S₁, NTD, or CTD-hFc recombinant

proteins were immobilized on protein A (ProA) biosensors (ForteBio, 18-5010). Subsequently, the biosensors were washed and incubated with twofold serial-diluted monomeric nanobodies (Twin-Strep Tag II only) in the kinetic buffer (PBST) to record the association kinetics, followed by recording the dissociation kinetics in the same kinetic buffer. The background was established using a kinetic buffer without the binding proteins. The kinetic parameters and binding affinities were determined using the Octet Data Analysis software (v.12.2.0.20) with global curve fitting using a 1:1 binding model.

VSV pseudovirus entry and inhibition assay

Single-round VSV-based pseudoviruses carrying the coronavirus spikes were produced following a modified version of a well-established protocol⁶⁷. The VSV-ΔG carrying GFP and firefly luciferase (VSV-ΔG-fLuc-GFP) was rescued using a reverse genetics system in the laboratory, along with helper plasmids (pBS-N, pBS-P, pBS-G, and pBS-L) from Karafast. For packaging coronavirus pseudovirus, HEK293T cells were transfected with plasmids overexpressing the spike proteins. At 24–36 hpt, cells were inoculated with 1 × 10⁶ TCID₅₀ ml⁻¹ VSV-dG-fLuc-GFP for 4 h at 37 °C with 8 μ g ml⁻¹ Polybrene. Following two DMEM washes, the culture medium was replenished with DMEM containing 1 μ g ml⁻¹ anti-VSV-G neutralizing antibody (from the I1-mouse hybridoma) to minimize background signals from parental viruses. The TCID₅₀ of the pseudovirus was calculated using the Reed–Muench method^{68,69}.

For pseudovirus entry or entry inhibition assays, susceptible cells were cultured in 96-well plates at a density of 5 × 10⁴ cells per well and then incubated with around 1 × 10⁶ TCID₅₀ ml⁻¹ of pseudovirus, with 100 μ l per well. The incubation allowed for attachment and viral entry with or without the indicated concentrations of antibodies or other inhibitors. In some cases, TPCK-treated trypsin (Sigma-Aldrich, T8802) at indicated concentrations was added to the medium to enhance entry efficiency. At 16–20 hpi, 40 μ l of One-Glo-EX substrate (Promega) was added to the cells and incubated for at least 5 min on a plate shaker in the dark. Relative light units (RLU) were determined using the GloMax 20/20 Luminometer (Promega). GFP intensity was analysed using a fluorescence microscope (Mshot, MI52-N).

Recombinant VSV-CoV propagation assay

For VSV-CoV propagation assays, the propagation-competent (pc) recombinant VSVs with VSV-G gene genetically replaced with HKU1, HKU3, or HKU5 spike genes (pcVSV-HKU1, pcVSV-HKU3, and pcVSV-HKU5) were generated by the VSV-based reverse genetics system. The vector for the VSV genomes was modified based on pVSV-ΔG-fLuc-GFP, with fLuc replaced by the coronavirus spike genes. In brief, the BHK-21 cells were infected with a recombinant vaccinia virus expressing T7 RNA polymerase (VVT7) for 45 min at 37 °C (MOI = 5). After removing VVT7, the cells were transfected with plasmids containing the pVSV-ΔG-GFP-HKU1/HKU3/HKU5-S vector and helper plasmids from Karafast. The virus-containing supernatant (PO) was collected 48 hpt and amplified in Vero E6 cells with *in trans*-provided VSV-G to yield P1 viruses. The P1 viruses were further amplified in Caco2-CVRs cells in a VSV-G independent manner and in the presence of anti-VSV-G (I1-Hybridoma supernatant), generating P2 viruses that were dependent on the genetically encoded coronavirus spike glycoproteins for amplification, which can be enhanced with the presence of 20 μ g ml⁻¹ TPCK-treated trypsin in DMEM + 2% FBS.

Production of recombinant spike glycoprotein

The prefusion SARS-CoV-2 spike ectodomain contains the Wuhan-Hu-1 sequence plus Hexapro stabilizing mutations (F817P, A892P, A899P, A942P, K986P and V987P), S₁/S₂ cleavage site mutations (R682G, R683S and R685S) as well as C-terminal foldon trimerization domain, 3 C cleavable His and Twin-Strep Tag II⁵⁰. For triggering assays, we used a construct encoding SARS-CoV-2 spike G614 with a mu-phosphatase signal peptide placed before spike residue Q14, with a mutated S₁/S₂

cleavage site (S_{682} GAR $_{685}$), and ending at residue K1211 followed by a TEV cleavage site, a foldon trimerization motif, and an 8× His tag cloned in a pCMV vector^{70,71}. Spike trimers were produced in 200-ml cultures of Expi293F Cells (Thermo Fisher Scientific) grown in suspension using Expi293 Expression Medium (Thermo Fisher Scientific) at 37 °C in a humidified 8% CO₂ incubator rotating at 130 rpm. Cells grown to a density of 3×10^6 cells per ml were transfected using the ExpiFectamine 293 Transfection Kit (Thermo Fisher Scientific) and cultivated for 5 days, at which point the supernatant was collected. Spike ectodomains were purified from clarified supernatant using a Cobalt affinity column (Cytiva, HiTrap TALON crude), washing with 20 column volumes of 50 mM Tris-HCl pH 8.0, 150 mM NaCl, and 1 mM imidazole, and eluted with 50 mM Tris-HCl pH 8.0, 150 mM NaCl, and 600 mM imidazole. The spike ectodomain was then concentrated using a 100-kDa centrifugal filter (Amicon Ultra 0.5-ml centrifugal filters, MilliporeSigma), residual imidazole was washed away by consecutive dilutions in the centrifugal filter unit with 50 mM Tris-HCl pH 8.0 and 150 mM NaCl, and finally concentrated to 1 mg ml⁻¹ for use immediately after purification.

Cryo-EM sample preparation and data collection

One-hundred microlitres of 1 mg ml⁻¹ prefusion-stabilized SARS-CoV-2 spike ectodomain was incubated with 2.2 µl of 67 mg ml⁻¹S2L20 Fab for 15 min at 37 °C. Most unbound Fab was then washed away with six consecutive dilutions in 400 µl of 50 mM Tris-HCl pH 8.0 and 150 mM NaCl and concentration using a 100-kDa centrifugal filter (Amicon Ultra 0.5-ml centrifugal filters, MilliporeSigma). The complex was concentrated to 3.5 mg ml⁻¹ and 3 µl was immediately applied onto a freshly glow-discharged 2.0/2.0 UltraFoil grid⁷² (200 mesh), plunge frozen using a vitrobot MarkIV (Thermo Fisher Scientific) using a blot force of -1 and 6.0 s blot time at 100% humidity and 23 °C. Data were acquired using the Leginon software⁷³ to control an FEI Titan Krios transmission electron microscope equipped with a Gatan K3 direct detector and operated at 300 kV with a Gatan Quantum GIF energy filter. The dose rate was adjusted to 3.75 counts per super-resolution pixel per s, and each movie was acquired in 75 frames of 40 ms with a pixel size of 0.843 Å and a defocus range comprised between -0.2 and -2.0 µm.

Cryo-EM data processing

Movie frame alignment (with a downsampled pixel size of 1.686 Å) was carried out using Warp⁷⁴. Estimation of the microscope contrast-transfer function parameters followed by manual micrograph curation, Blob particle picking, particle extraction (with a box size of 256 pixels²), reference-free 2D classification to generate templates for template-based particle picking (templates and micrographs low-pass filtered to 20 Å resolution during template-based particle picking), particle re-extraction, and then reference-free 2D classification were performed in cryoSPARC⁷⁵. Well-defined particle images ab initio reconstruction followed by non-uniform 3D refinement in CryoSPARC⁷⁶ before subjecting particle images to Bayesian polishing using Relion⁷⁷ during which particles were re-extracted with a box size of 512 Å at a pixel size of 0.843 Å. Reference-free 2D classification and non-uniform refinement in CryoSPARC followed by Bayesian polishing in Relion was repeated. At this stage, 3D classification with 50 iterations each (angular sampling 7.5° for 25 iterations and 1.8° with local search for 25 iterations) was carried out using Relion without imposing symmetry⁷⁸. Next, 42 optics groups were defined based on the beam tilt angle used for data collection, and another round of non-uniform refinement in CryoSPARC was then performed concurrently with defocus refinement and Global CTF refinement, fitting beam-tilt and trefoil⁷⁹. For focused classification of the NTD, particles were symmetry-expanded and 3D classified in Relion without alignment using a mask that encompasses the NTD and the S2L20 V_H/V_L region. Particles in well-defined 3D classes were then used for local refinement in CryoSPARC. Reported resolutions are based on the gold-standard Fourier shell correlation of 0.143 criterion

and Fourier shell correlation curves were corrected for the effects of soft masking by high-resolution noise substitution^{80,81}.

Cryo-EM model building and analysis

UCSF Chimera⁸² and Coot⁸³ were used to fit atomic models of S2L20 and SARS-CoV-2 spike (PDB 7SOB and 7LXY) into the cryo-EM maps. The model was then refined and rebuilt into the map using Coot⁸³, Rosetta^{84,85}, and ISOLDE⁸⁶. Model validation and analysis used MolProbity⁸⁷, EMRinger⁸⁸, Privateer⁸⁹ and Phenix version 1.21⁹⁰. Figures were generated using UCSF ChimeraX⁹¹.

Triggering assay

For antibody-triggered spike refolding, 20 µl of 0.21 mg ml⁻¹SARS-CoV-2 spike G614 ectodomain (without 2P or Hexapro stabilizing mutations) was incubated at 37 °C for 1 h with and without 0.21 mg ml⁻¹ S2H14, S2X28, or S2L20, immediately prior to negative staining. Samples were diluted to 0.01 mg ml⁻¹ immediately prior to adsorption to glow-discharged carbon-coated copper grids for 30 sec prior to staining with 2% uranyl formate. Micrographs were recorded using the Leginon software⁷³ on a 120 kV FEI Tecnai G2 Spirit with a Gatan Ultrascan 4000 4k × 4k CCD camera at 67,000 nominal magnification. The defocus ranged from -1.0 to -2.0 µm and the pixel size was 1.6 Å.

Cell-cell fusion assays

A cell-cell fusion assay based on dual split proteins was performed on HEK293T or Caco2 cells stably expressing the CVRs or the native receptors¹³. Group A cells were transfected (Lipofectamine 2000, Biosharp) with plasmids expressing spike proteins and RLuc (residues 1–155)-sfGFP (residues 1–157), while the group B cells were transfection with plasmids expressing spike proteins (same as in group A) and sfGFP (residues 158–231)-RLuc(residues 156–311). Cells from both groups were trypsinized and co-cultured in a 96-well plate at a density of approximately 1×10^5 cells per well at 12 hpt. After 24 h, cells were washed once with DMEM to remove FBS. Following incubation of DMEM with or without 100 µg ml⁻¹ of TPCK-treated trypsin at 37 °C for 15 min, and subsequent culture in DMEM + 10% FBS for 24–36 h, cell nuclei were stained with Hoechst 33342 (1:5,000 dilution in HBSS) for 30 min at 37 °C, and then analysed by fluorescence imaging using a fluorescence microscope (M1S2-N; Mshot). For the assessment of live-cell luciferase activity after reconstitution of split RlucN, 20 µM of EnduRen live-cell substrate (Promega, E6481) was added to the cells in DMEM and incubated for at least 1 h before detection using the Varioskan LUX Multi-well Luminometer (Thermo Fisher Scientific).

Flow cytometry analysis

For live-cell binding assays analysing CoVs S_I/RBD-mFc recombinant proteins binding, proteins were diluted in DMEM at the indicated concentrations and then incubated with HEK293T cells expressing the CVRs for 1 h at 37 °C, followed by incubation with Alexa Fluor 594-conjugated goat anti-mouse IgG (Thermo Fisher Scientific; A32742; 1:5,000) to detect antigen binding and Alexa Fluor 488-conjugated goat anti-human IgG (Thermo Fisher Scientific; A11013; 1:5,000) to detect CVRs (with cell surface hFc) expression. If hFc was absent, the intracellular Flag tags were utilized to assess the receptor expression. Specifically, cells were washed once with HBSS and fixed with 4% paraformaldehyde (PFA), permeabilized with 0.1% Triton X-100, blocked with 1% BSA/PBS at 4 °C for 30 min, and subsequently stained with rabbit anti-Flag tag monoclonal antibody (CST, 14793S; 1:1,000) diluted in 1% BSA/PBS for 1 h at 4 °C. Following extensive washing, the cells were incubated with Alexa Fluor 647-conjugated goat anti-rabbit IgG (Thermo Fisher Scientific; A32733; 1:5,000) and Alexa Fluor 488-conjugated goat anti-mouse IgG (Thermo Fisher Scientific; A32723; 1:5,000) for 1 h at 4 °C for detecting both Flag tags and SARS-CoV-2 spike RBD-mFc binding.

For scFv-mFc binding assays, the SARS2-CoV-2 spike IRES-ZsGreen expressing cells were incubated with indicated concentrations of

Article

scFv-mFc for 1 h at 37 °C in DMEM/1% BSA, washed once with PBS, and then incubated with Alexa Fluor 594-conjugated goat anti-mouse IgG (Thermo Fisher Scientific; A32742; 1:5,000). For 76E1 epitope exposure assays, the SARS-CoV-2 spike IRES-ZsGreen expressing cells were first incubated with scFv-mFc or soluble ACE2 for 1 h in DMEM/1% BSA, washed once and then incubated with 76E1 (1 µg ml⁻¹) at 37 °C for another hour in DMEM/1% BSA. Subsequently, the washed cells were incubated with DyLight 594-conjugated goat anti-human IgG (Thermo Fisher Scientific; SA5-10136; 1:5,000) to detect 76E1 binding.

After all staining procedures, cells were washed twice with PBS and then analysed using the CytoFLEX Flow Cytometer (Beckman). In each case, 5,000 cells expressing either receptors or spikes, gated based on Flag, hFc or ZsGreen-fluorescence and SSC or FSC, were analysed with the CytoFLEX Flow Cytometer (Beckman). FlowJo (version 10) was used to analyse the flow cytometry data. The representative gating strategies for each experiment are demonstrated in Supplementary Fig. 3.

HKU5 reverse genetics

The full-length cDNA clone of HKU5 (strain: HKU5-1LMH03f, GenBank: NC_009020) was designed and synthesized as seven (from A to G) contiguous cDNAs flanked by unique class IIIS restriction endonuclease site (Bsal or BsmBI) and cloned in pUC57 vector. Class II restriction endonuclease sites AvrII and Ascl were introduced to the 5' terminus of HKU5 A and the 3' terminus of HKU5 G fragments, respectively. Several silent mutations were included to disrupt naturally occurring restriction cleavage sites. A poly-A (25 repeats) sequence was introduced to the 3' terminus of the HKU5 G fragment. To assemble the full-length cDNA clone, HKU5 A-G fragments were digested by endonucleases, resolved on 1% agarose gels, purified with a gel extraction kit, extracted with chloroform, and precipitated with isopropyl alcohol. Digested HKU5 A-G inserts, and modified pBalobAC11 vector were mixed, ligated overnight at 4 °C, and transformed into DH10B competent cells. The correct full-length HKU5 cDNA clone was identified and verified by sequencing. The construction of HKU5-ZGH utilized the transformation-associated recombination cloning technique. Specifically, a ZsGreen-HiBiT-encoding DNA fragment was commercially synthesized (Tsingke) to replace the HKU5-ORF5. The PCC1 vector was used to clone the HKU5 genomic DNA carrying the ZGH substitution based on three segments amplified using the HKU5-wild-type (WT) infectious clone as a temperate. Subsequently, all the products were transformed into yeast using the high-efficiency lithium acetate/SS carrier DNA/PEG method. The yeast plasmid was extracted and transformed into EPI300 electrocompetent cells. The plasmid used for cell transfection was obtained from a 300 ml *Escherichia coli* bacterial culture suspension. For transfection, 4 µg of HKU5-WT and HKU5-ZGH plasmids were separately transfected into Caco2-1B4 cells (1 × 10⁶ cells) using GeneTwin (Biomed, TG101). Progeny viruses collected from the supernatant at 72 hpt (P0) were utilized to generate stocks for subsequent analyses.

HKU5 sampling and isolation

Bats were trapped in their natural habitat as previously described^{92,93}. An anal swab (sample ID: NL140575) with confirmed HKU5 genomic sequence (strain HKU5_PaGD2014/15) was collected from a *Pipistrellus abramus* bat in Guangzhou City, Guangdong province on 28 June 2014. The sample was preserved in viral transport medium (VTM) comprising HBSS, BSA (1%), amphotericin (15 µg ml⁻¹), penicillin G (100 U ml⁻¹) and streptomycin⁹⁴ (50 µg ml⁻¹), transported to the laboratory and stored at -80 °C until use. All bats trapped for this study were released back to their habitat after anal swab collection. All sampling processes were carried out by veterinarians with approval from the Animal Ethics Committee of the Wuhan Institute of Virology (WIVH05210201).

To isolate the HKU5, the sample preserved in VTM was centrifuged at 10,000g at 4 °C for 10 min. Then, 100 µl of the 0.45 µm-filtered sample was mixed with 100 µl DMEM + 2% FBS + 2× pen/strep and incubated with Caco2-1B4 cells at 37 °C for 2 h. This was followed by

supplementation of 400 µl fresh DMEM + 2% FBS + 2× pen/strep. The cytopathic effect was monitored daily, and the supernatant (passage 1, P1) was collected on day 5 post-infection. Subsequently, 200 µl of the P1 supernatant was incubated with freshly plated Caco2-1B4 cells at 37 °C for 1 h. The inocula were then removed and replenished with 400 µl fresh DMEM with 2% FBS. The HKU5-containing supernatant (passage 2, P2) was collected on day 3 and day 6 post-infection and stored at -80 °C. The Caco2 or Caco2-1B4 cells were challenged with P2 supernatant (collected on day 6) and fixed with methanol for 40 min at room temperature on day 3 post-infection, and HKU5 N proteins were detected by rabbit anti-HKU5 N protein serum (diluted at 1:4,000), followed by Cy3-conjugated goat anti-rabbit IgG (Abcam, 1:250) staining. All HKU5 isolation-related experiments were conducted in the certified negative-pressure Biosafety Level 2 laboratory at the Wuhan Institute of Virology (WIV).

Transmission electron microscopy

Viral culture supernatant was fixed with formaldehyde (working concentration 0.1%) at 4 °C overnight. Subsequently, it was concentrated by ultracentrifugation through OptiPrep™ Density Gradient Medium (D1556) at 154,000g at 4 °C for 2.5 h using a SW41Ti rotor (Beckman). The pelleted viral particles were suspended in 100 µl of PBS, stained with 2% phosphotungstic acid (pH 7.0), and examined using a transmission electron microscope (Thermo Fisher, Talos L120C) at 120 kV.

Authentic coronavirus infection assays

Human coronavirus 229E (VR740) was obtained from ATCC and amplified in Huh-7 cells. MHV-A59 was a gift from the laboratory of Y. Chen and was amplified in Neuro2a cells. The SARS-CoV-2 (ΔN-GFP) with N protein substituted with GFP was rescued using an established protocol, and was cultured in Caco2 cells overexpressing the SARS-CoV-2 N protein⁹⁵. All experiments involving RsHuB2019A, and HKU5-related authentic viruses infection were conducted in the certified negative-pressure Biosafety Level 2 laboratory at WIV. RsHuB2019A is amplified in either Huh-7 or in Caco2-Nb27 cells. HKU5-related strains are amplified in Caco2-1B4 cells.

For authentic virus infection assays, target cells were seeded in 24-well plates, washed once with DMEM, and then inoculated with the indicated MOI of authentic viruses for 1 h. Subsequently, the infected cells were washed with DMEM once and replenished with DMEM with or without 2% FBS. RsHuB2019A infection was conducted in Huh-7 cells in DMEM (must be FBS-free) with 100 µg ml⁻¹ trypsin (Sigma-Aldrich, T4549). RsHuB2019A or HKU5-1 infection in Caco2-CVR cells was conducted with or without the presence of 100-200 µg ml⁻¹ trypsin (in DMEM + 2% FBS) or 5-10 µg ml⁻¹ trypsin (in DMEM without FBS) during and post-inoculation. For RT-qPCR analysis of viral RNA accumulation, cell-free supernatants (50 µl per well each time) were collected at indicated time points post-infection and stored at -80 °C. Viral RNA was extracted using Virus DNA/RNA Extraction Kit (Vazyme: RM501) and subjected to RT-qPCR as previously described⁹⁶. RT-qPCR was conducted using the C1000 Touch Thermal Cycler/CFX96 Real-time system (Bio-Rad) and analysed with Bio-Rad CFX Maestro (4.1.2433.1219) software. Primers for RsHuB2019ARdRp: 5'-TTGTTCTTGCTCGAAACATA-3' (forward) and 5'-CACACATGACCATCTCACTTA-3' (reverse). Primer for HKU5 nsp2: 5'-CTGGCCTTAATGCCCATTC-3' (forward) and 5'-GACGTGTAGACGTAGAGCCG-3' (reverse). Primers for VSV L protein, forward primer: 5'-TCTTGAGTTGTGGAGACGGC-3' (forward) and 5'-ACCGCTTGAACATGGGACC-3' (reverse). Primers for MHV-A59 N protein: 5'-TATAAGACTGATTGGCGTCC-3' (forward) and 5'-GAGTAATGGGAACCACACT-3' (reverse). All samples were analysed in duplicate on two independent runs.

For immunofluorescence assays, cells were fixed with 4% PFA for at least 20 min at 25 °C for 24–48 hpi at specified time points. N proteins for RsHuB2019A and HKU5 were detected using rabbit anti-Rp3 N protein serum (1:2,000) and rabbit anti-HKU5 N protein serum

(1:4,000), respectively, followed by Cy3-conjugated goat anti-rabbit IgG (Abcam, 1:250) staining. Images were captured using an EVOS M5000 fluorescence microscope (Thermo Fisher Scientific). For MHV-A59 and 229E-VR740, spike proteins were detected using their spike-targeting nanobodies (1A1-mFc for 229E-VR740; 1F7-mFc for MHV-A59), followed by DL594-conjugated goat anti-mouse IgG antibodies (Thermo Fisher, 1:1,000). Images were captured and merged using a fluorescence microscope (Mshot, MI52-N). The titre of the authentic viruses was determined by immunofluorescence at 4 days post-infection, and the TCID₅₀ was calculated using the Reed–Muench method^{68,69}.

Nanobody biopanning

Specific viral antigens (30–100 µg) were immobilized on streptavidin-conjugated magnetic beads for one-hour incubation at 37 °C and extensively washed to remove unbound antigens. Subsequently, the beads were incubated with the nanobody library (1×10^{10} PFU) (naive VHH libraries from Camelus bactrianus, Alpaca, and Llama from NBbiolab) for 1 h. The bound phages were eluted using an elution buffer (50 mM Tris-pH 7.4, 150 mM NaCl, 50 mM biotin) after extensive washing with PBST to eliminate nonspecific binders. The eluted phage encoding the specific nanobodies was proliferated in *E. coli* (TG1). After one round of magnetic beads-based selection, one to three additional rounds of phage biopanning were conducted using magnetic beads or immunotubes. The positive clones were identified through enzyme-linked immunosorbent assays, sequenced and verified by cell-based binding assays. Nanobody information is summarized in Supplementary Table 3.

Biosafety statement

Experiments related to authentic human coronavirus 229E, SARS-CoV-2-ΔN and MHV-A59 were authorized by the Biosafety Committee of the State Key Laboratory of Virology, Wuhan University and conducted in accordance with standard operating procedures (SOPs) in a BSL-2 laboratory. SARS-CoV-2 authentic viruses-related experiments were conducted in the ABSL-3 facility at Wuhan University with the approval of the Biosafety Committee of the ABSL-3 laboratory. The SARS-CoV-2 wild-type strain (IVCAS 6.7512) was provided by the National Virus Resource, WIV, Chinese Academy of Sciences and amplified in Vero E6 cells in the ABSL-3 facility at Wuhan University. Experiments related to authentic viruses RsHuB2019A, HKU5-WT and HKU5-ZGH were approved by the WIV institutional biosafety committees and performed in the BSL-2 laboratory according to SOPs at WIV facilities. In vitro experiments related to RsHuB2019A infection, HKU5-1(LMH03f) rescue, and HKU5 (PaGD2014/15 strains) isolation were performed in the BSL-2 laboratory following SOPs with necessary personal protection and approved by the WIV institutional biosafety committee according to a biorisk assessment procedure. In vitro experiments involving these bat coronaviruses were assessed as BSL-2 level primarily based on their narrow cell tropism and limited efficiency in using human receptors. The complete assessment includes the viral genome sequence and its phylogenetic relationship to known human viruses, human receptor utilization, cell tropism, prevalence in domestic animals and humans, and pathogenicity and transmission in animal models. All the facilities at both Wuhan University and WIV for this work adhere strictly to the safety requirements recommended by the China National Accreditation Service for Conformity Assessment.

We recommend that future research activities involving the use of CVR-expressing cells to isolate, rescue or propagate uncharacterized authentic viruses should be authorized first and strictly adhere to biosafety requirements based on the biorisk assessment conducted by the institutional Biosafety Committee on a case-by-case basis, in accordance with the biosafety regulations of different countries. We recommend experiments based on pseudoviruses or replication-deficient viruses be conducted first whenever possible to gather essential data

for biorisk assessment before isolating or rescuing authentic viruses. Considering the potential mutations during the propagation of viruses in human cells, biological feature changes during passages should be closely monitored and viral genome sequencing should be conducted to check whether key adaptive mutations occurred. Furthermore, non-human cells expressing CVR can also be used for virus propagation to minimize the risk of viruses adapting to human cells. Large-scale viral propagation of the newly isolated/rescued uncharacterized viruses and initial virus characterization in animal models are suggested to be performed in a BSL-3 containment. The biorisk classification and containment levels of previously uncharacterized viruses should be re-assessed based on newly acquired data related to the biological and epidemiological characterizations to comply with the biosafety regulations of the country.

Bioinformatic and computational analyses

Multi-sequence alignment was analysed by Mafft (v7.313) and Geneious Prime (2023.0.1) with default parameters. Phylogenetic trees were constructed by IQ-TREE (v2.0.6) with the WAG substitution model (1,000 Bootstraps) and rendered with iTOL (v6) (<http://itol.embl.de>).

Statistical analysis and reproducibility

Most experiments were repeated independently 2–4 times with similar results, each with approximately 2–4 biologically independent replicates (most are $n = 3$). Results are presented as mean \pm s.d. as specified in the figure legends. Statistical analyses were primarily performed using GraphPad Prism (Version 8.0.2) through unpaired two-tailed Student's *t*-tests for two independent groups or one-way ANOVA followed by Dunnett's test for multiple comparisons. No adjustments were made for all multiple comparisons. $P < 0.05$ was considered statistically significant; * $P < 0.05$; ** $P < 0.01$; *** $P < 0.001$; **** $P < 0.0001$; NS, non-significant, $P > 0.05$.

Reporting summary

Further information on research design is available in the Nature Portfolio Reporting Summary linked to this article.

Data availability

The cryo-EM maps and models have been deposited to the Electron Microscopy Data Bank and Protein Data Bank (PDB) with accession numbers EMD-45174 and 9C44 (global refinement of the S2L20-bound spike trimer), and EMD-45175 and 9C45 (local refinement of the NTD and S2L20 Fab variable regions). The accession numbers (NCBI GenBank or GISAID) and protein sequence information of receptor, virus, antibodies, domains and reporter genes are provided in the Methods and supplementary tables. All other data supporting the findings of this study are available with the Article and the Supplementary Information. All reagents generated in this study are available from H.Y. with a completed materials transfer agreement. Source data are provided with this paper.

64. Loo, L. et al. Fibroblast-expressed LRRC15 is a receptor for SARS-CoV-2 spike and controls antiviral and antifibrotic transcriptional programs. *PLoS Biol.* **21**, e3001967 (2023).
65. Schwegmann-Weber, C. et al. Comparison of vesicular stomatitis virus pseudotyped with the S proteins from a porcine and a human coronavirus. *J. Gen. Virol.* **90**, 1724–1729 (2009).
66. Du, Y. et al. A broadly neutralizing humanized ACE2-targeting antibody against SARS-CoV-2 variants. *Nat. Commun.* **12**, 5000 (2021).
67. Whitt, M. A. Generation of VSV pseudotypes using recombinant ΔG-VSV for studies on virus entry, identification of entry inhibitors, and immune responses to vaccines. *J. Virol. Methods* **169**, 365–374 (2010).
68. Nie, J. et al. Quantification of SARS-CoV-2 neutralizing antibody by a pseudotyped virus-based assay. *Nat. Protoc.* **15**, 3699–3715 (2020).
69. Reed, L. J. & Muench, H. A simple method of estimating fifty per cent endpoints. *Am. J. Epidemiol.* **27**, 493–497 (1938).
70. Lemp, F. A. et al. Lectins enhance SARS-CoV-2 infection and influence neutralizing antibodies. *Nature* **598**, 342–347 (2021).

71. Bowen, J. E. et al. SARS-CoV-2 spike conformation determines plasma neutralizing activity elicited by a wide panel of human vaccines. *Sci. Immunol.* **7**, eadff1421 (2022).
72. Russo, C. J. & Passmore, L. A. Electron microscopy: ultrastable gold substrates for electron cryomicroscopy. *Science* **346**, 1377–1380 (2014).
73. Suloway, C. et al. Automated molecular microscopy: the new Legion system. *J. Struct. Biol.* **151**, 41–60 (2005).
74. Tegunov, D. & Cramer, P. Real-time cryo-electron microscopy data preprocessing with Warp. *Nat. Methods* **16**, 1146–1152 (2019).
75. Punjani, A., Rubinstein, J. L., Fleet, D. J. & Brubaker, M. A. cryoSPARC: algorithms for rapid unsupervised cryo-EM structure determination. *Nat. Methods* **14**, 290–296 (2017).
76. Punjani, A., Zhang, H. & Fleet, D. J. Non-uniform refinement: adaptive regularization improves single-particle cryo-EM reconstruction. *Nat. Methods* **17**, 1214–1221 (2020).
77. Zivanov, J., Nakane, T. & Scheres, S. H. W. A Bayesian approach to beam-induced motion correction in cryo-EM single-particle analysis. *IUCrJ* **6**, 5–17 (2019).
78. Zivanov, J. et al. New tools for automated high-resolution cryo-EM structure determination in RELION-3. *eLife* **7**, e42166 (2018).
79. Zivanov, J., Nakane, T. & Scheres, S. H. W. Estimation of high-order aberrations and anisotropic magnification from cryo-EM data sets in ~31. *IUCrJ* **7**, 253–267 (2020).
80. Rosenthal, P. B. & Henderson, R. Optimal determination of particle orientation, absolute hand, and contrast loss in single-particle electron cryomicroscopy. *J. Mol. Biol.* **333**, 721–745 (2003).
81. Chen, S. et al. High-resolution noise substitution to measure overfitting and validate resolution in 3D structure determination by single particle electron cryomicroscopy. *Ultramicroscopy* **135**, 24–35 (2013).
82. Pettersen, E. F. et al. UCSF Chimera—a visualization system for exploratory research and analysis. *J. Comput. Chem.* **25**, 1605–1612 (2004).
83. Emsley, P., Lohkamp, B., Scott, W. G. & Cowtan, K. Features and development of Coot. *Acta Crystallogr. D* **66**, 486–501 (2010).
84. Wang, R. Y.-R. et al. Automated structure refinement of macromolecular assemblies from cryo-EM maps using Rosetta. *eLife* **5**, e17219 (2016).
85. Frenz, B. et al. Automatically fixing errors in glycoprotein structures with Rosetta. *Structure* **27**, 134–139.e3 (2019).
86. Croll, T. I. ISOLDE: a physically realistic environment for model building into low-resolution electron-density maps. *Acta Crystallogr. D* **74**, 519–530 (2018).
87. Chen, V. B. et al. MolProbity: all-atom structure validation for macromolecular crystallography. *Acta Crystallogr. D* **66**, 12–21 (2010).
88. Barad, B. A. et al. EMRinger: side chain-directed model and map validation for 3D cryo-electron microscopy. *Nat. Methods* **12**, 943–946 (2015).
89. Aguirre, J. et al. Privaterer: software for the conformational validation of carbohydrate structures. *Nat. Struct. Mol. Biol.* **22**, 833–834 (2015).
90. Liebschner, D. et al. Macromolecular structure determination using X-rays, neutrons and electrons: recent developments in Phenix. *Acta Crystallogr. D* **75**, 861–877 (2019).
91. Goddard, T. D. et al. UCSF ChimeraX: meeting modern challenges in visualization and analysis. *Protein Sci.* **27**, 14–25 (2018).
92. Li, W. et al. Bats are natural reservoirs of SARS-like coronaviruses. *Science* **310**, 676–679 (2005).
93. Hu, B. et al. Discovery of a rich gene pool of bat SARS-related coronaviruses provides new insights into the origin of SARS coronavirus. *PLoS Pathog.* **13**, e1006698 (2017).
94. Ge, X.-Y. et al. Isolation and characterization of a bat SARS-like coronavirus that uses the ACE2 receptor. *Nature* **503**, 535–538 (2013).
95. Ju, X. et al. A novel cell culture system modeling the SARS-CoV-2 life cycle. *PLoS Pathog.* **17**, e1009439 (2021).
96. Guo, H. et al. ACE2-independent bat sarbecovirus entry and replication in human and bat cells. *mBio* **13**, e0256622 (2022).

Acknowledgements The authors are grateful for the funding support from the Basic Science Center Program of the National Natural Science Foundation of China (NSFC) (32188101 to H.Y.), National Key R&D Program of China (2023YFC2605500 to Z.-L.S. and H.Y.), NSFC Excellent Young Scientists Fund (82322041 to H.Y.), other NSFC projects (32270164, 32070160 to H.Y., 323B2006 to C.-B.M. and 32300141 to H.G.), Fundamental Research Funds for the Central Universities (2042023kf0191 and 2042022kf1188 to H.Y.), and Natural Science Foundation of Hubei Province (2023AFA015 to H.Y.), and China Postdoctoral Science Foundation (2023M733708 to H.G.). This study was also supported by the National Institute of Allergy and Infectious Diseases (P01AI167966, DP1AI158186 and 75N93022C00036 to D.V.), an Investigators in the Pathogenesis of Infectious Disease Awards from the Burroughs Wellcome Fund (D.V.), the University of Washington Arnold and Mabel Beckman CryoEM center and the National Institute of Health grant S10OD032290 (to D.V.). D.V. is an Investigator of the Howard Hughes Medical Institute and the Hans Neurath Endowed Chair in Biochemistry at the University of Washington. The authors thank X.-X. Wang for providing the human sera collected post-vaccination (SARS-CoV-2 CoronaVac, Sinovac) and collected by Beijing Youan Hospital (approval number LL-2021-042-K); K. Cai for providing sera collected from Wuhan COVID-19 convalescents (identification number 2021-012-01); Z.-H. Qian for providing BANAL-20-52 related spike-expressing plasmids; L. Lu for providing EK1-related peptides; P. Zhang and B.-C. Xu for their help with the ultracentrifugation and electron microscopic analysis; Y.-J. Li for assisting in establishing the yeast cloning methods; Y. Chen for providing the MHV-A59 strain; C.-G Wu for assisting in isolating the HKU5_PaGD2014/15 stain; Q. Ding for providing the SARS-CoV-2 (ΔN-GFP) reverse genetics related plasmids; and K. Lan and the ABSL-3 facility and other core facilities of the Key Laboratory of Virology, Wuhan University.

Author contributions H.Y., P.L., M.-L.H., H.G. and M.M. conceived the study and designed the experiments. J.L. conducted the first experiment of this study. P.L., M.-L.H., H.G., M.M., J.-Y.S., Y.-M.C., C.-L.W., X. Yu, C.L., L.-L.S., Y.-h.S., X. Yang and J.L. established the assays and methods, designed and cloned receptor and protein constructs and conducted related experiments. P.L., M.-L.H., C.-L.W., L.-L.S., C.-B.M., Q.X., F.T. and C.L. screened the nanobodies. P.L., M.-L.H. and L.-L.S. conducted 229E and MHV authentic virus-related experiments at Wuhan University. P.L. and H.G. conducted the RShuB2019A and HKU5 negative staining for electron microscopy imaging at the Wuhan Institute of Virology. J.C. and P.L. constructed the infectious clones of HKU5 and HKU5-ZGH, respectively. M.G. conducted the SARS-CoV-2 authentic virus infection-related experiments in ABSL-III at Wuhan University. M.M. carried out cryo-EM sample preparation, data collection and processing of the S2L20-bound SARS-CoV-2 spike dataset. M.M. and D.V. built and refined the structure. M.M. and J.E.B. carried out antibody-mediated triggering assays. D.C. provided critical reagents. H.Y., Z.-L.S., D.V., P.L., M.-L.H., M.M., C.-L.W. and X. Yu analysed the data. H.Y., P.L. and M.-L.H. prepared the original draft of the manuscript. H.Y., D.V., Z.-L.S., P.L. and M.-L.H. revised the manuscript with input from all other authors. H.Y., Z.-L.S. and D.V. obtained funding to support this study. H.Y. supervised the project.

Competing interests H.Y. has submitted a patent application to the China National Intellectual Property Administration for the utilization of artificial viral receptors and their applications.

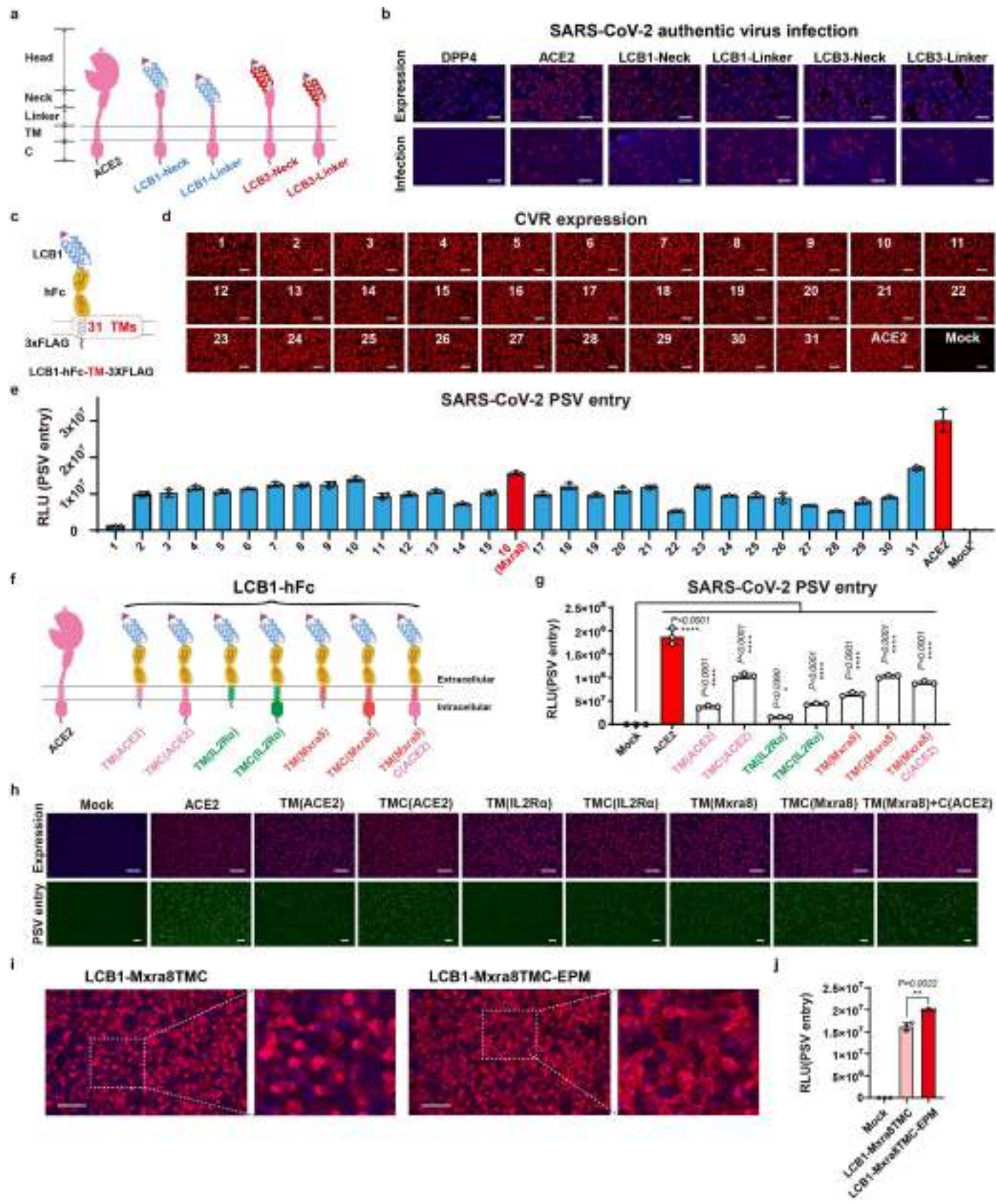
Additional information

Supplementary information The online version contains supplementary material available at <https://doi.org/10.1038/s41586-024-08121-5>.

Correspondence and requests for materials should be addressed to David Veesler, Zheng-Li Shi or Huan Yan.

Peer review information *Nature* thanks Shibo Jiang and the other, anonymous, reviewer(s) for their contribution to the peer review of this work.

Reprints and permissions information is available at <http://www.nature.com/reprints>.



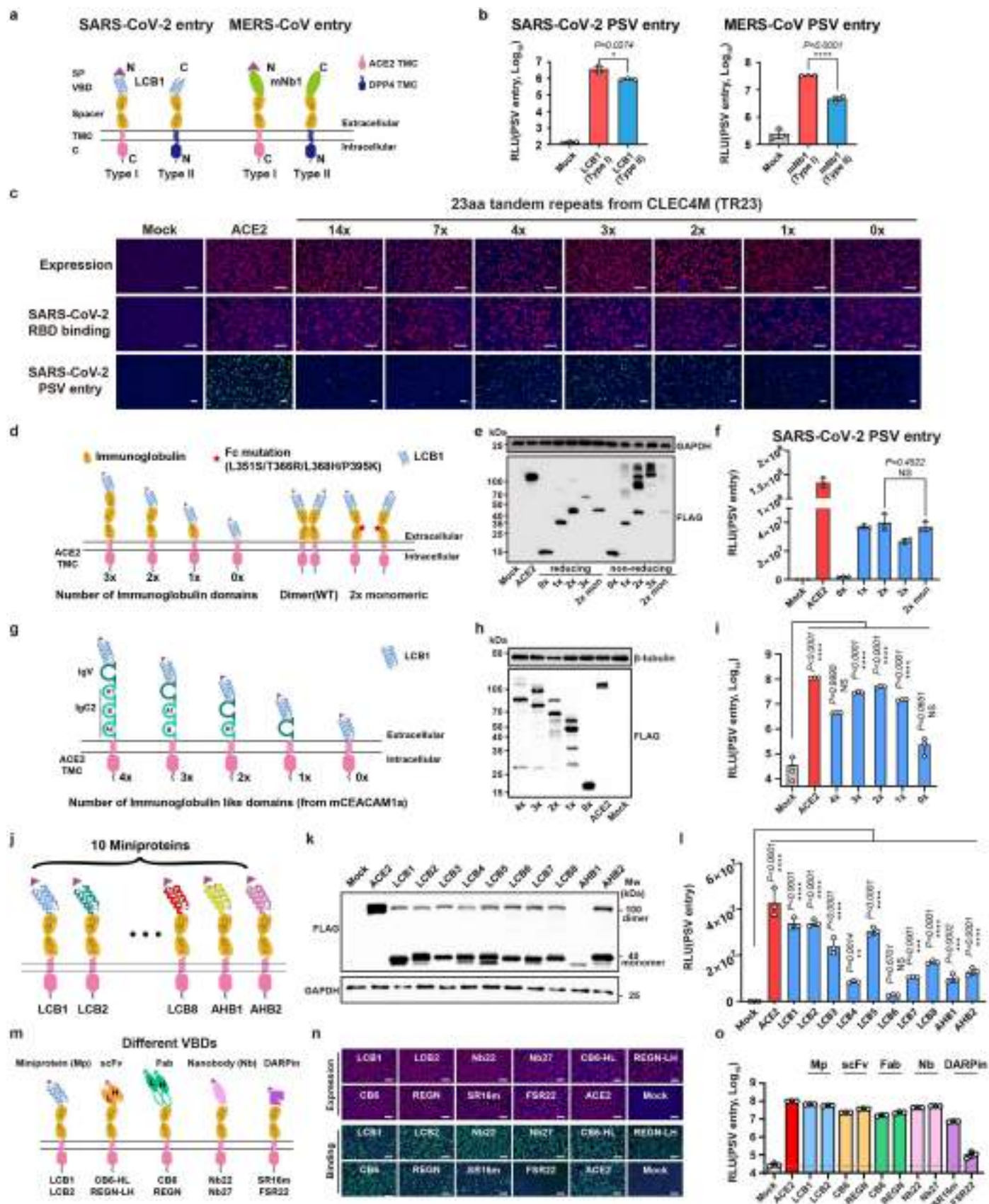
Extended Data Fig. 1 | See next page for caption.

Article

Extended Data Fig. 1 | Development and optimization of a modular design strategy for CVR with a type I transmembrane topology. **a**, Schematic illustration of the four miniprotein-based CVRs. **b**, Immunofluorescence analysis of ACE2/CVRs expression and authentic SARS-CoV-2 infection in HEK293T cells stably expressing the receptors. Upper: Receptor expression examined by C-terminal fused 3×Flag tags. Lower: SARS-CoV-2 infection efficiency as indicated by intracellular N proteins at 24 hpi. Data representative of two independent authentic SARS-CoV-2 infection assays with similar results. **c**, Cartoon illustrating the framework of the CVRs for TM evaluation. **d**, Immunofluorescence analysis of the expression of the 31 CVRs in HEK293T cells by detecting the C-terminal fused 3×Flag tags. **e**, SARS-CoV-2 PSV entry efficiency promoted by CVRs carrying different TMs. The detailed information on the TMs is summarized in Supplementary Table 2. Data are presented as mean ± s.d. ($n = 3$ wells of independently infected cells), representative of two independent experiments with similar results. **f**, Schematic diagram showing

the LCB1-based CVRs with indicated TM or TMC substitutions. **g, h**, SARS-CoV-2 PSV entry in HEK293T cells transiently expressing the indicated CVRs examined by RLU (g) or GFP (h). Data are presented as mean ± s.d. ($n = 3$ wells of independently infected cells). Statistical analysis was performed using One-way ANOVA analysis followed by Dunnett's test. Data represented were performed in at least two independent experiments with similar results.

i, Immunofluorescence analysis of the subcellular distribution of LCB1-MXRA8 TMC-based CVRs with or without EPM transiently expressed in HEK293T cells. The white dashed boxes highlight the cell surface distribution with a higher magnification. **j**, SARS-CoV-2 PSV entry efficiency in HEK293T cells transiently expressing CVRs with or without EPM. Data are mean ± s.d. ($n = 3$ wells of independently infected cells) and analyzed with unpaired two-tailed Student's *t*-tests, representative of two independent experiments with similar results. Scale bars: 100 μm in **b, d, h**, and **i**. * $P < 0.05$, ** $P < 0.01$, **** $P < 0.0001$.

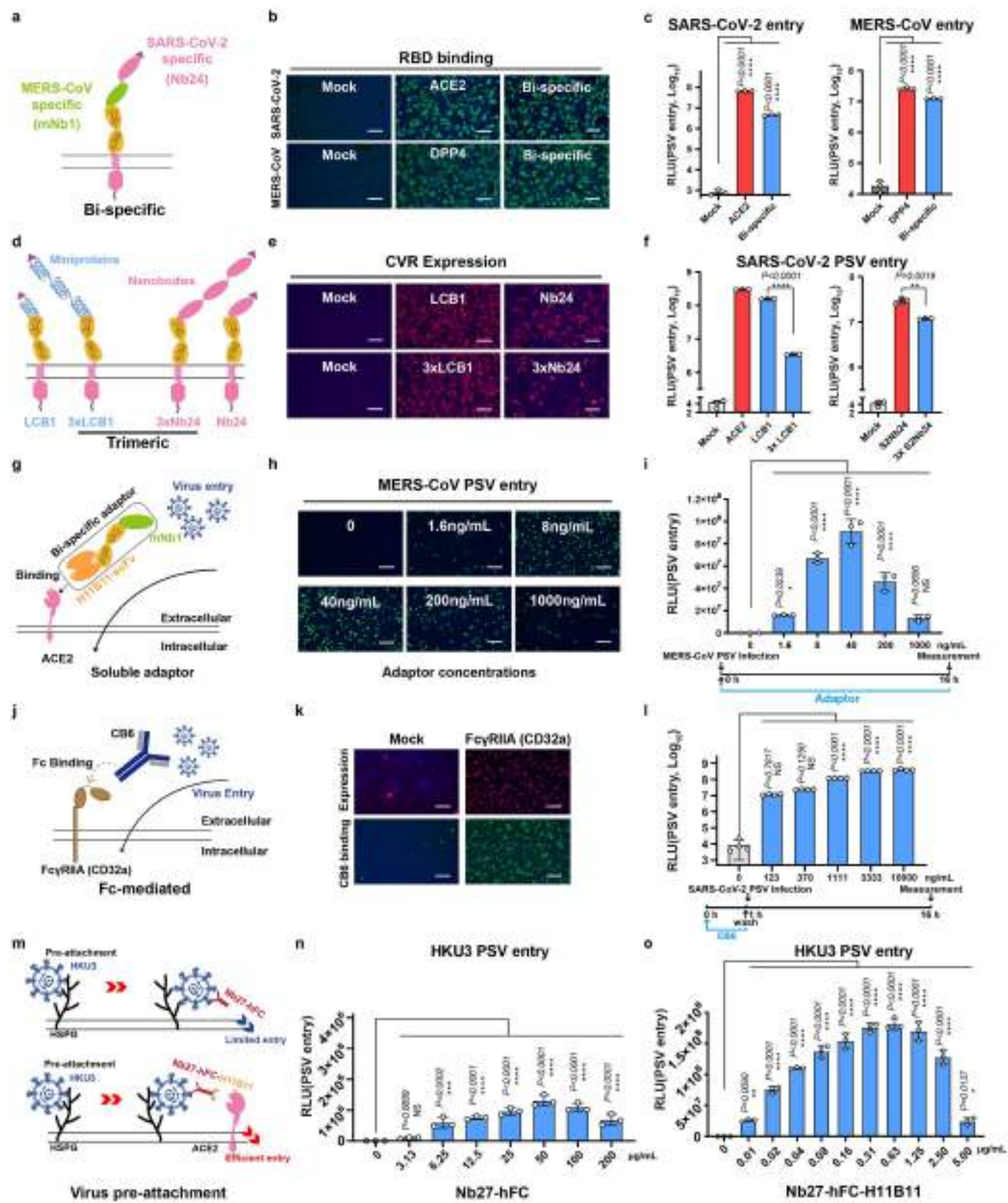


Extended Data Fig. 2 | See next page for caption.

Article

Extended Data Fig. 2 | Exploring factors that contribute to the receptor function of CVRs with different topologies or modules. **a**, Schematic diagram showing CVRs carrying LCB1 or mNb1 displayed in either type I or type II transmembrane topology. **b**, Evaluation of SARS-CoV-2 or MERS-CoV PSV entry efficiency supported by the indicated CVRs with different transmembrane topologies in HEK293T cells. Data are mean \pm s.d. of biological triplicates examined over three independent infection assays. Unpaired two-tailed Student's *t*-tests. **c**, Assessment of CVR expression, SARS-CoV-2 RBD-mFc binding, and PSV entry efficiency supported by the CVRs carrying varying copies of TR23 repeats transiently expressed in HEK293T cells. Data are representative of three independent experiments. Scale bars: 100 μ m. **d**, Schematic representation of the CVRs carrying different numbers of immunoglobulin (Ig) domains (left) or an Fc mutant with abolished dimerization ability. **e**, Western blot analysis of CVRs expression in HEK293T cells under either reducing or non-reducing conditions, respectively. **f**, Assessment of SARS-CoV-2 PSV entry efficiency in HEK293T cells transiently expressing the indicated CVRs. Data are mean \pm s.d. ($n = 3$ wells of independently infected cells.) and analyzed by unpaired two-tailed Student's *t*-tests. **g**, Schematic representation of the CVRs carrying different numbers of Ig-like domains (left)

from mCEACAM1a. **h**, Western blot analysis of CVRs expression in HEK293T cells. **i**, SARS-CoV-2 PSV entry efficiency in HEK293T cells transiently expressing the indicated CVRs. Data are mean \pm s.d. ($n = 3$ wells of independently infected cells). One-way ANOVA analysis followed by Dunnett's test. **j**, Schematic representation of the CVRs carrying different SARS-CoV-2 RBD targeting miniproteins. **k**, **l**, Expression (**k**) and SARS-CoV-2 entry-supporting (**l**) ability of different CVRs in 293T cells. Data are mean \pm s.d. ($n = 3$ wells of independently infected cells). One-way ANOVA analysis followed by Dunnett's test. **m**, Schematic diagram showing CVRs carrying different types of VBDs, the two representative VBDs for each type are indicated. **n**, Immunofluorescence analyzing the expression of the indicated CVRs transiently expressed in HEK293T cells by detecting the C-terminal fused 3 \times Flag tags, and the SARS-CoV-2 RBD binding. Scale bars: 100 μ m. **o**, PSV entry are supported by indicated CVRs transiently expressed in HEK293T cells. Data are mean \pm s.d. ($n = 3$ wells of independently infected cells). Data representative of two independent transfections, expression verification, and infection assays with similar results for **d-f**, **g-i,j-l**, and **m-o**, respectively. * $P < 0.05$, ** $P < 0.01$, *** $P < 0.001$, **** $P < 0.0001$; NS, Not significant ($P > 0.05$).

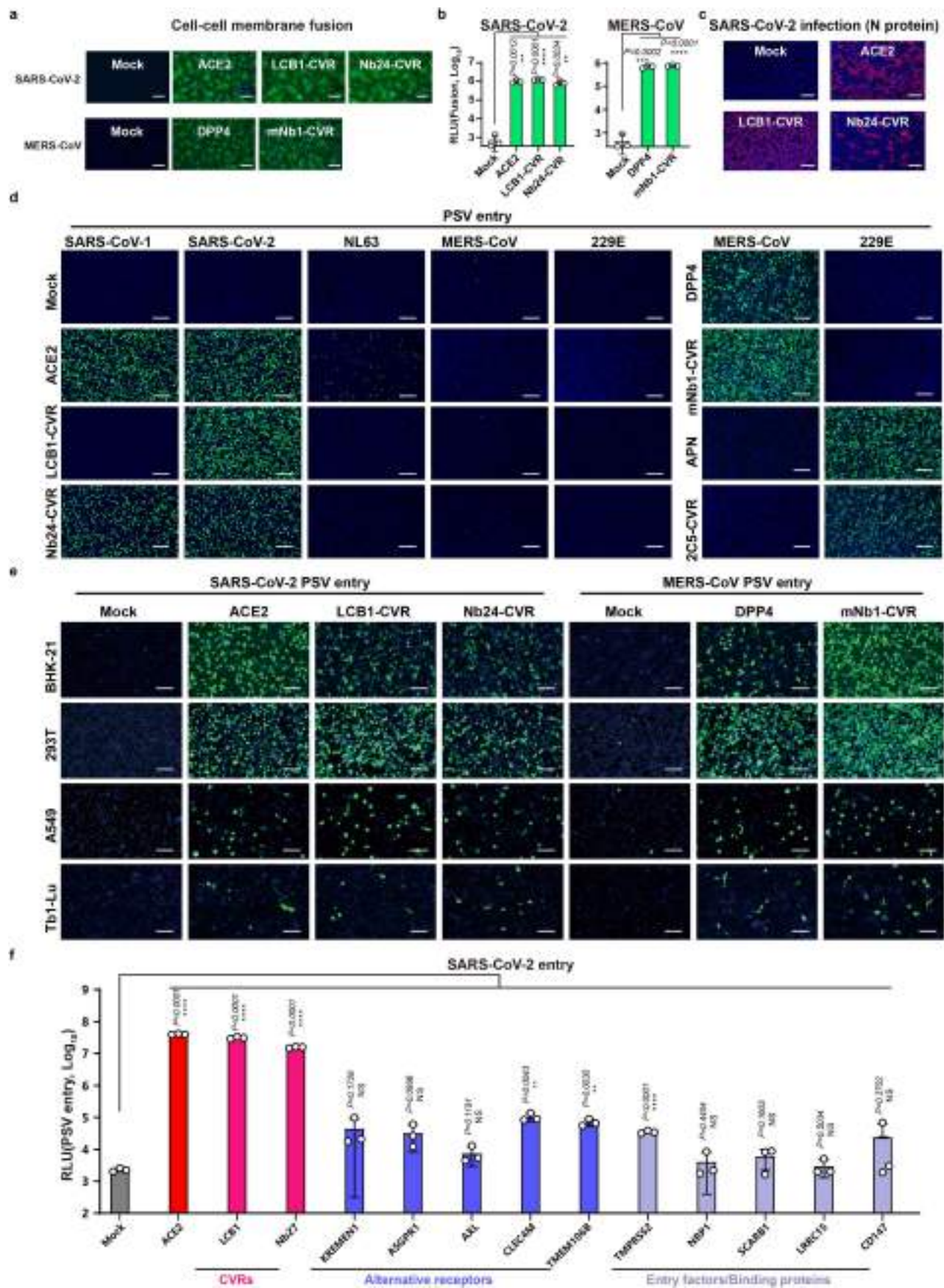


Extended Data Fig. 3 | See next page for caption.

Article

Extended Data Fig. 3 | Investigating receptor function of CVRs with VBDs connected in various ways. **a-c**, Illustration (a), RBD binding efficiency (**b**), and PSV entry-supporting efficiency (**c**) of a SARS-CoV-2/MERS-CoV bi-specific CVR transiently expressed in HEK293T cells. Data are presented as mean \pm s.d. (biological triplicates of infected cells), representative of three independent experiments with similar results. Unpaired two-tailed Student's *t*-test. **d-f**, Illustration (**d**), expression (**e**), and PSV entry-supporting efficiencies (**f**) of CVRs carrying single or trimeric VBD. Data are mean \pm s.d. (biological triplicates of infected cells), analyzed by unpaired two-tailed Student's *t*-test. Representative of two independent experiments. **g-i**, Schematic illustration of bispecific adapter protein (**g**) and MERS-CoV PSV entry efficiency in BHK-21-hACE2 cells in the presence of indicated concentrations of adapter proteins (h11B11-mNb1) throughout the infection. Entry efficiency is examined by GFP intensity (**h**) or RLU (**i**). Data are mean \pm s.d. (biological triplicates of infected cells), representative of three independent infection assays. **j-l**, Schematic

illustration of Fc γ R (CD32a) mediated antibody-dependent coronavirus entry (**j**). CD32a expression, antibody (CB6) binding (**k**), and SARS-CoV-2 PSV entry (**l**) into HEK293T-CD32a cells pretreated with indicated concentration (con.) of the CB6 antibodies. Data are mean \pm s.d. ($n = 4$ wells of biologically independent cells), examined over two independent experiments. **m-o**, Entry of pre-attached PSV promoted by soluble neutralizing antibody (Nb27-hFc) or bi-specific neutralizing antibody with membrane-associating ability (Nb27-hFc-h11B11). Schematic illustration (**m**), Nb27-hFc promoted entry (**n**), and Nb27-hFc-h11B11 promoted PSV entry (**o**) in Caco2 cells with virus pre-attachment by 1500 rpm centrifugation at 4 °C for 1 h. Data are mean \pm s.d. (biological triplicates of infected cells). Data are representative of three independent infection assays. Scale bars: 100 μm for **b**, **e**, and **k**, and 200 μm for **h**. One-way ANOVA analysis followed by Dunnett's test for **i**, **l**, **n**, and **o**. * $P < 0.05$, ** $P < 0.01$, *** $P < 0.001$, **** $P < 0.0001$; NS, Not significant ($P > 0.05$).



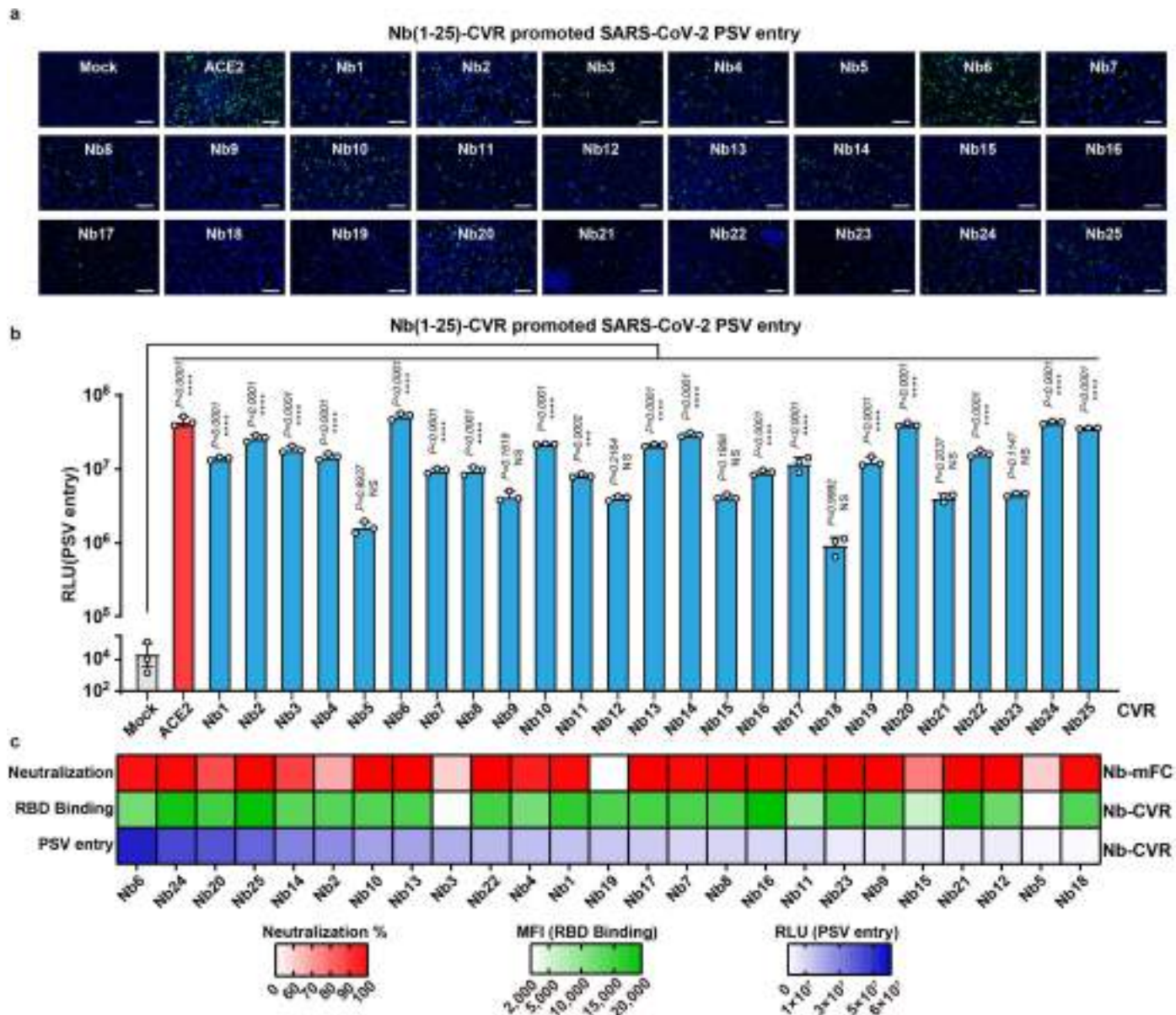
Extended Data Fig. 4 | See next page for caption.

Article

Extended Data Fig. 4 | Comparing receptor function of CVRs with native receptors, or alternative receptors/coreceptors in different cell types.

a-c, The ability of CVRs to promote cell-cell membrane fusion, and authentic SARS-CoV-2 infection is comparable to their native receptors. Spike and receptor-mediated cell-cell fusion was demonstrated by reconstituted GFP intensity (**a**) and relative light unit (RLU) of Renilla luciferase activity (**b**). Authentic SARS-CoV-2 infection was examined by immunostaining of intracellular N proteins at 24 hpi (**c**). Data are mean \pm s.d. (biological triplicates) for **b**. Data are representative of two independent fusion assays or infection

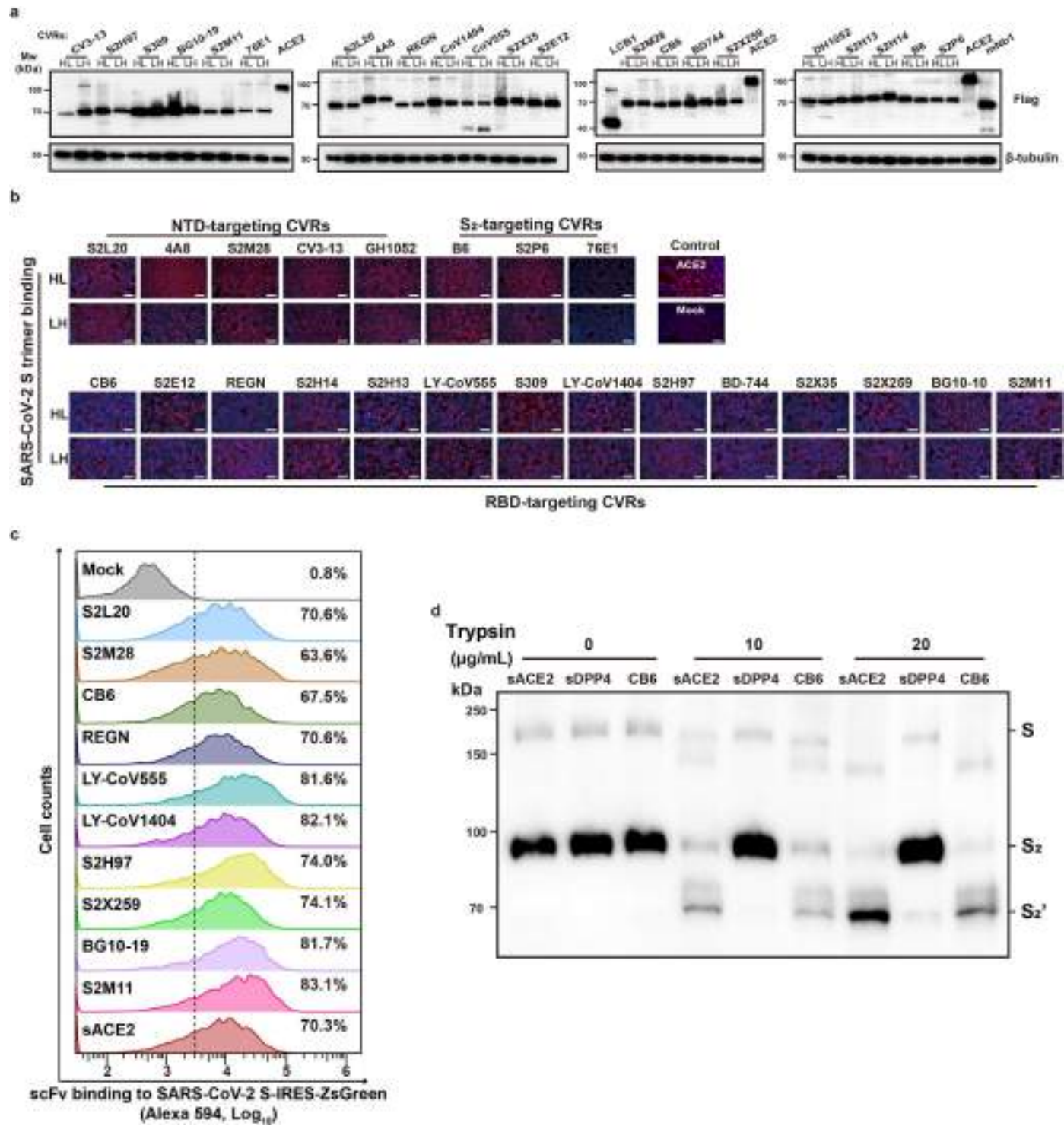
assays with similar results. **d**, Receptor specificity of different coronavirus PSVs in HEK293T stably expressing the native receptor or the indicated CVRs. **e**, SARS-CoV-2 and MERS-CoV PSV entry into various cell types expressing the indicated receptors. Data representative of two independent transfection and infection assays with similar results for **d** and **e**. **f**, SARS-CoV-2 PSV entry efficiencies in HEK293T cells expressing different receptors or entry factors. Data are presented as mean \pm s.d. ($n = 3$ wells of independently infected cells.), representative of two independent transfection and infection experiments. ** $P < 0.01$, *** $P < 0.001$, **** $P < 0.0001$; NS, Not significant ($P > 0.05$).



Extended Data Fig. 5 | Relationship between the binding affinity, neutralizing activity, and CVR entry-promoting efficiency of 25 SARS-CoV-2 RBD-targeting nanobody-fused receptors. **a, b,** Assessment of the entry-promoting ability of 25 nanobody-CVRs in HEK293T cells, indicated by GFP (**a**) and the RLU (**b**), respectively. Data are presented as mean \pm s.d. ($n = 3$ wells of independently infected cells), representative of two independent experiments. One-way ANOVA analysis followed by Dunnett's test. Scale bars: 200 μ m. **c,** Comparing RBD binding, neutralization, and PSV entry-promoting

ability of different nanobody-fused proteins in HEK293T cells. RBD-mFc binding and PSV entry assays were conducted in HEK293T transiently expressing the 25 nanobody-CVRs. The SARS-CoV-2 PSV neutralization assay was performed in HEK293T-ACE2 in the presence of indicated nanobody-Fc recombinant proteins (10 μ g ml $^{-1}$). Data are representative results of two independent experiments with similar results and plotted by the mean ($n = 3$ wells of independently infected/bound cells). *** $P < 0.001$, **** $P < 0.0001$; NS, Not significant ($P > 0.05$).

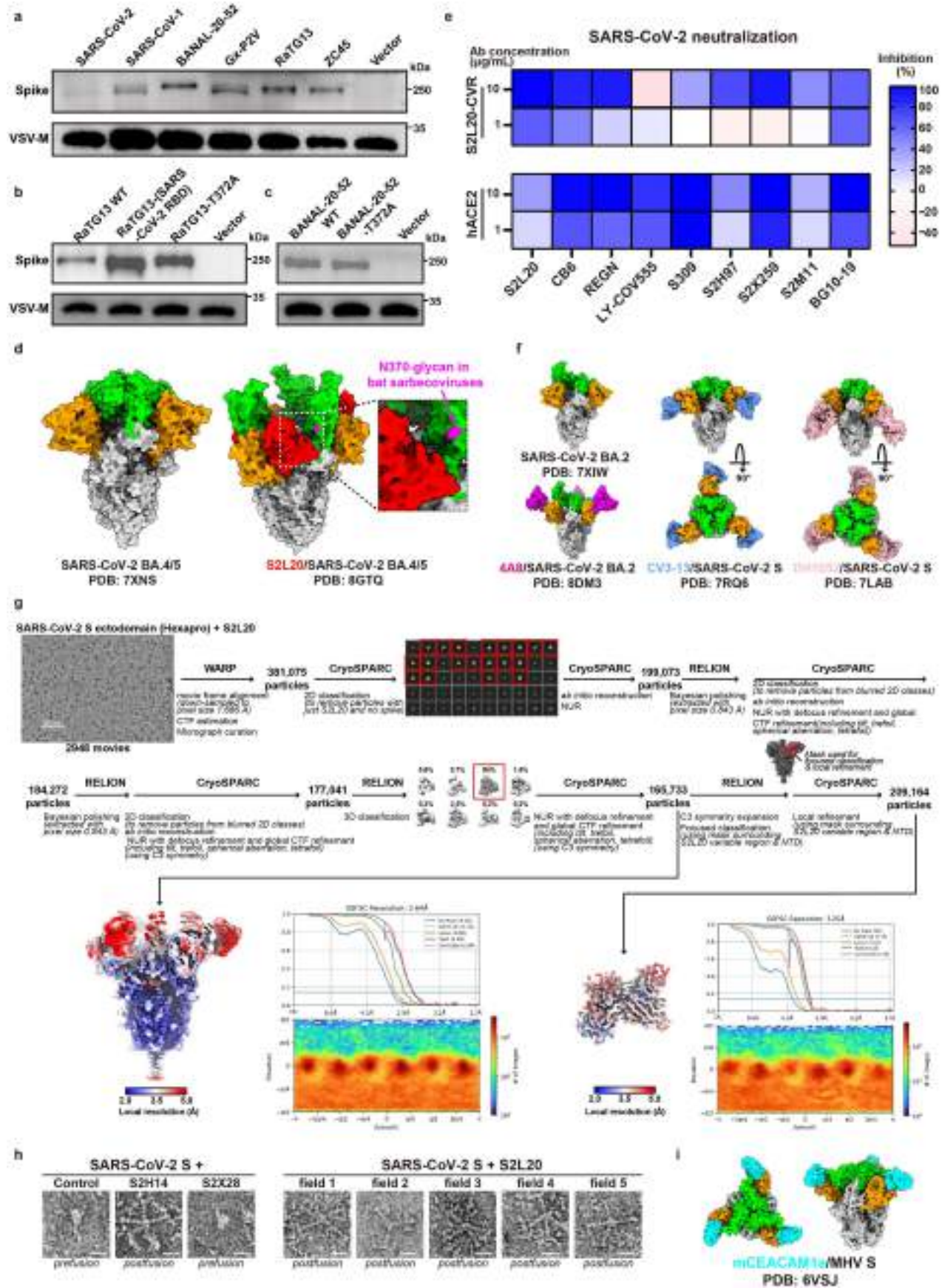
Article



Extended Data Fig. 6 | Expression and antigen-binding ability of CVRs targeting distinct SARS-CoV-2 neutralizing epitopes. **a**, Western blot analysis of the expression levels of indicated scFv-CVRs transiently expressed in HEK293T cells. Data are representative of two independent experiments. **b**, Binding of SARS-CoV-2 S-trimer to HEK293T cells expressing the indicated CVRs. Data are representative of three assays using independent preparations of proteins. **c**, Flow cytometry analysis of the binding efficiency of scFv-mFc with HEK293T cells transiently expressing the SARS-CoV-2 Spike proteins and ZsGreen simultaneously. The ZsGreen positive cells were gated for subsequent

analysis of mFc binding efficiency. Data representative from a single experiment with mean values ($n = 3$ wells of biologically independent cells) indicated.

d, Trypsin-mediated S_{2'} cleavage of S2S-CoV-2 PSV in the presence of soluble receptors or CB6-scFv-mFc. The concentrated SARS-CoV-2 PSV particles were incubated with 100 μ g ml⁻¹ of soluble receptors or CB6-scFv-mFc for 1 h, followed by incubation with the indicated concentration of TPCK-treated trypsin for 30 min. Western blot analysis was conducted by detecting the S2P6 epitope in the S₂ subunit. Data are representative of three independent assays with similar results.



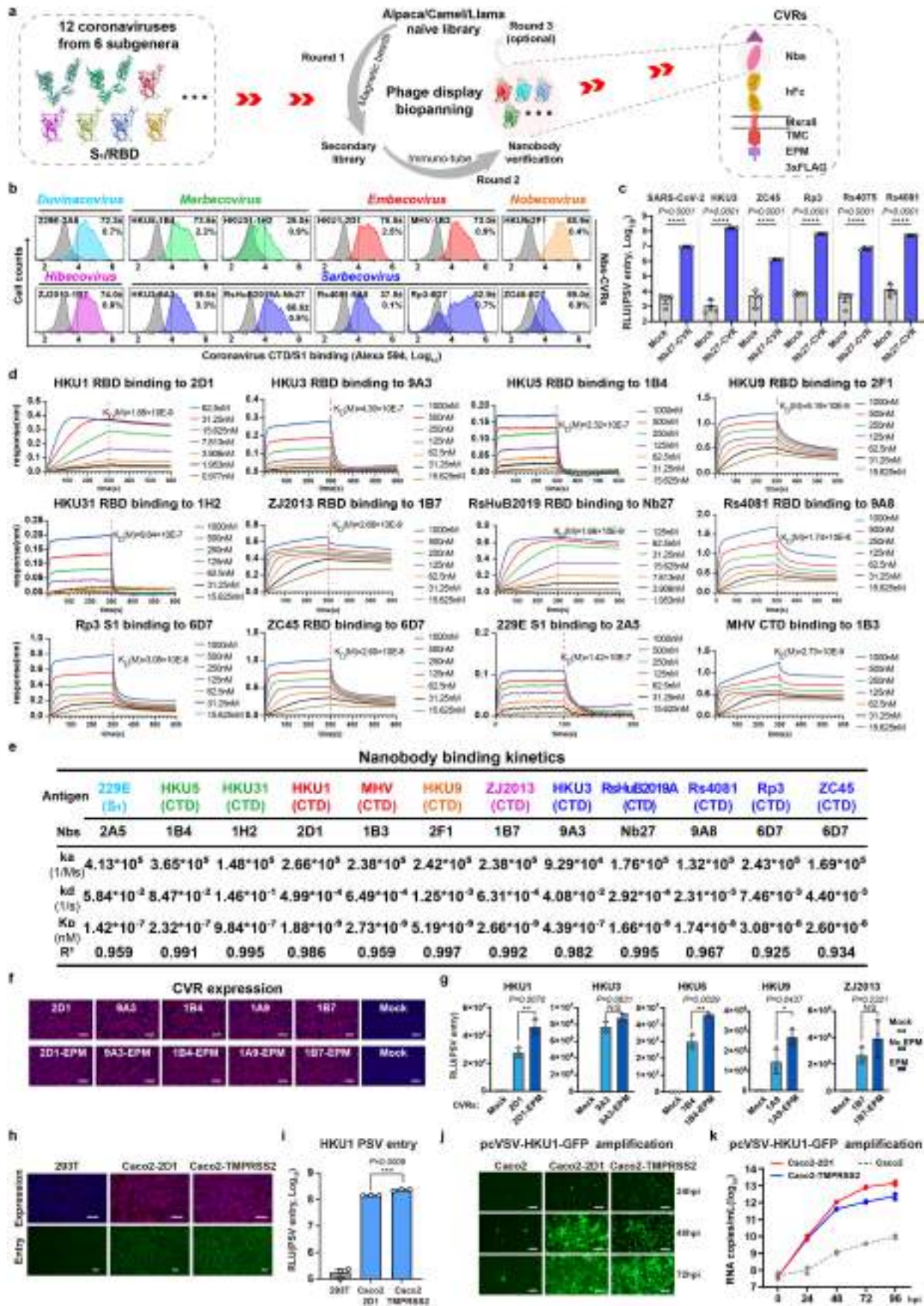
Extended Data Fig. 7 | See next page for caption.

Article

Extended Data Fig. 7 | Molecular basis of NTD-mediated coronavirus entry.

a-c, Package efficiency of PSVs carrying indicated sarbecoviruses spike glycoproteins (**a**) and the indicated mutants (**b, c**). Western blot was conducted by detecting the conserved S2P6 epitope. VSV-M serves as a loading control. Blots representative of two independent transfection assays for pseudovirus production. **d**, Structures of SARS-CoV-2 BA.4/5 spike trimer without antibody binding (left), or in complex with S2L20 (right). Dashed boxes highlighted the N370-glycan spatially proximate to the S2L20. **e**, Heatmap showing the inhibitory efficacy of indicated SARS-CoV-2 neutralizing antibodies against PSV entry in HEK293T-hACE2 or HEK293T-S2L20, with BSA as a control. Data are representative results of two independent neutralization assays and plotted by the mean ($n = 3$ wells of independently infected cells). **f**, Structures of SARS-CoV-2 BA.2 spike trimers with (upper) or without (lower) the binding

of NTD-targeting 4A8, along with the side-view (top) and top-view (bottom) cryoEM structures of SARS-CoV-2 Wuhan-Hu-1 spike trimers with the binding of NTD-targeting CV3-13 and DH1052. Orange: NTD; Green: CTD; Red: S2L20; Magenta: 4A8; Blue: CV3-13; Pink: DH1052. **g**, CryoEM data processing workflow and validation of the S2L20-bound SARS-CoV-2 S CryoEM structure. **h**, Negative stain microscopy of prefusion SARS-CoV-2 S-glycoprotein (without stabilizing proline substitutions) incubated without antibody, or with S2H14, S2X28, or S2L20 as indicated. S2H14 is known to promote the transition to the postfusion state and was used as a control³⁷. Scale bars: 10 nm. Data representative of images captured from two independent experiments with similar results. **i**, Top-view and side-view CryoEM structures depicting soluble mCEACAM1a (cyan) in complex with MHV spike trimer (gray). NTD and CTD of MHV S are indicated in orange and green, respectively.

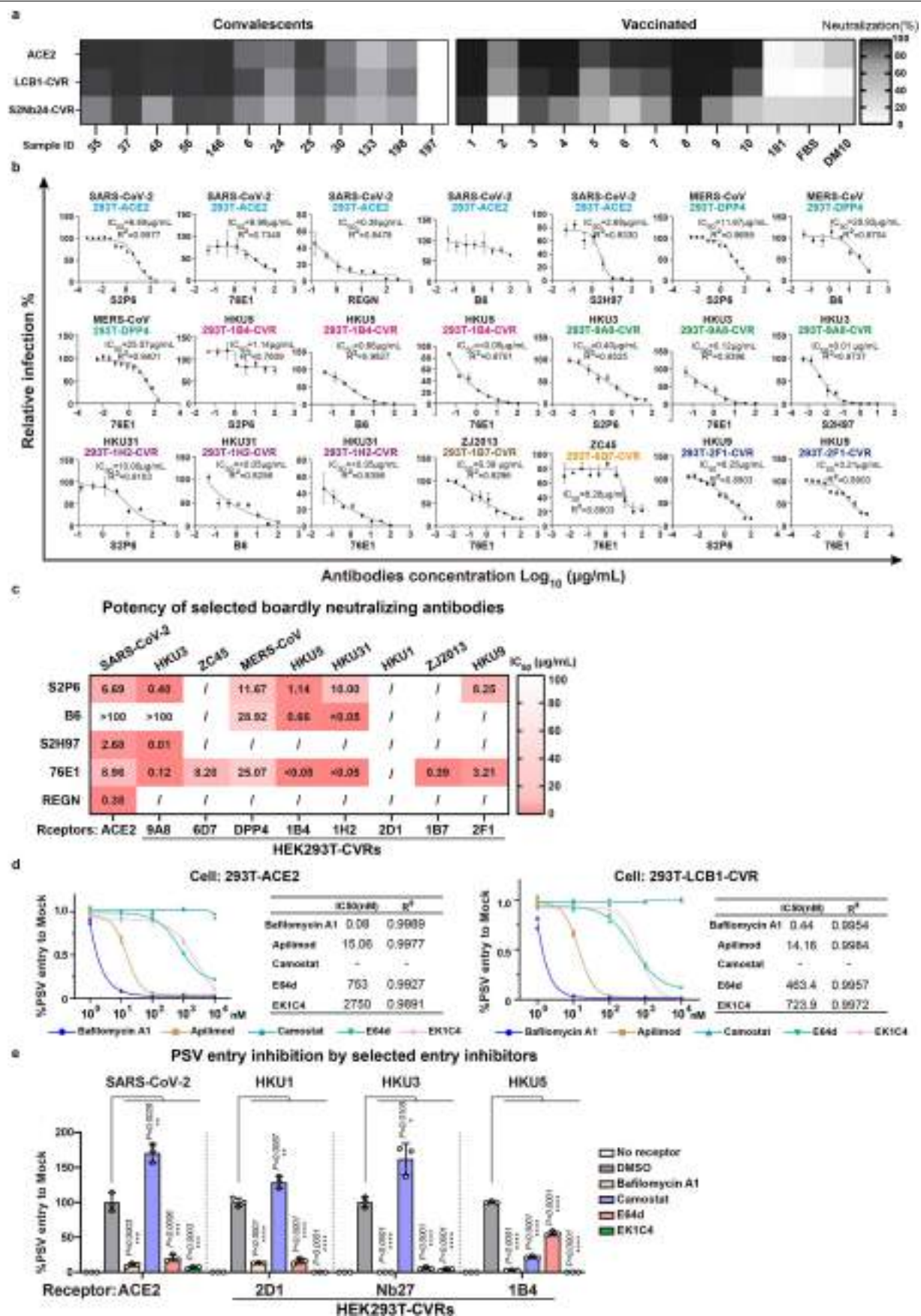


Extended Data Fig. 8 | See next page for caption.

Article

Extended Data Fig. 8 | Generation and characterization of VBDs used for CVRs customized for various coronaviruses. **a**, Workflow demonstrating the customization of nanobody-based CVRs for specific coronaviruses. **b**, Coronavirus CTD or S_i binding in HEK293T cells transiently expressing the corresponding CVRs. Dashed lines indicate thresholds for positive ratio calculation. Data are presented as mean \pm s.d. ($n = 3$ wells of biologically independent cells), representative of two independent experiments. **c**, The pan-sarbecovirus entry-promoting ability of CVR-Nb27 was evaluated by six different sarbecoviruses in 293T cells. Data are presented as mean \pm s.d. (biological quadruples of infected cells), representative of two independent infection assays. Unpaired two-tailed Student's *t*-tests. **d**, BLI analyses of binding kinetics of immobilized RBD and S_i-hFc (for 229E) of the indicated coronaviruses with the indicated monomeric nanobodies. **e**, a summary of binding kinetics of nanobodies bound to the immobilized virus antigens. **f,g**, Expression (**f**) and entry-supporting efficiency (**g**) of the CVRs with or

without EPM transiently expressed in the HEK293T cells. EPM: endocytosis prevention motif. Data are mean \pm s.d. ($n = 3$ independently infected cells). Unpaired two-tailed Student's *t*-tests. Experiments were performed twice with similar results, and representative data were shown. **h-k**, HKU1 specific 2D1-CVR exhibited a comparable receptor function to TMPRSS2. The expression (**h**) and HKU1-PSV entry promoting efficiency (**i**, **j**) of the two receptors were examined. The amplification of propagation-competent rSV-HKU1-GFP in Caco2 cells expressing 2D1-CVR and TMPRSS2 was demonstrated by GFP (**j**) and RNA accumulation (**k**). Scale bars: 100 μ m for **f**, **h**, and **j**. Data are mean \pm s.d. ($n = 3$ biologically independent wells of cells) analyzed by unpaired two-tailed Student's *t*-tests for **i**. Data presented are RNA copies of two independently infected cells with each point representing the mean of technical duplicates (RT-qPCR) for **k**. Experiments presented were independently performed twice with similar results for **h-j** and single time for **k**. * $P < 0.05$, ** $P < 0.01$, *** $P < 0.001$, **** $P < 0.0001$; NS, Not significant ($P > 0.05$).

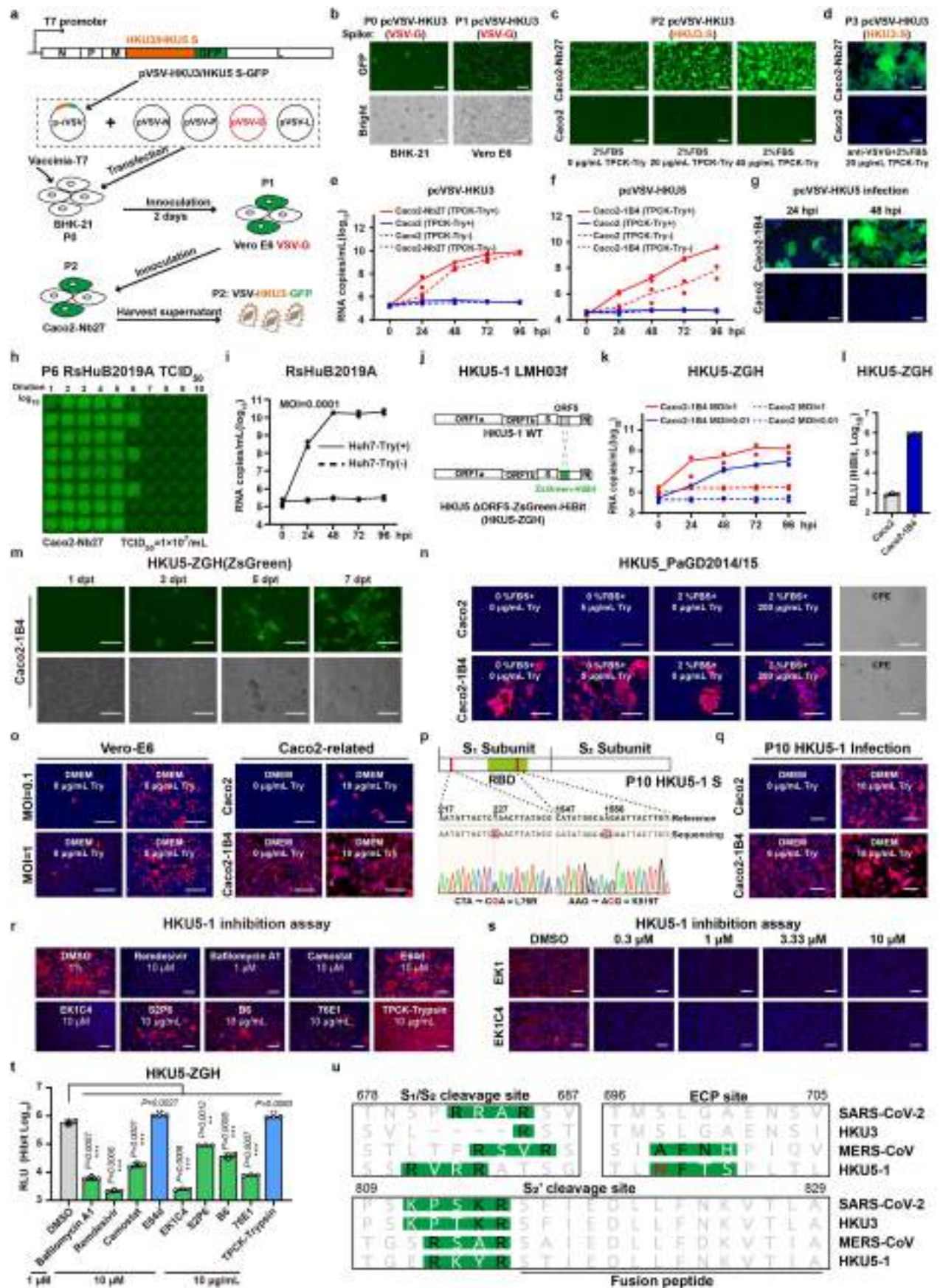


Extended Data Fig. 9 | See next page for caption.

Article

Extended Data Fig. 9 | Neutralization and inhibition assays based on CVR-expressing HEK293T cells. **a**, Comparison of neutralization profiles of sera collected from COVID-19 convalescents (left) or vaccinated individuals (right) based on HEK293T cells expressing ACE2 or two different CVRs. Serum dilution: 1:200. Heatmap plotted by the mean values (biologically triplicates of infected cells), which are representative results out of two independent experiments. **b, c**, Neutralization assays of several broadly neutralizing antibodies against PSV entry of representative coronaviruses in HEK293T stably expressing the indicated CVRs. Neutralization curves (**b**) and a summary of IC₅₀ (**c**) against each virus are shown. The RBD-targeting REGN19033 (REGN)

was employed as a control. /: no inhibition detected. Data are mean ± s.d. (biologically triplicates of infected cells). **d**, The IC₅₀ of selected entry inhibitors against SARS-CoV-2 PSV entry was determined in both HEK293T-ACE2 or HEK293T-LCBI-CVR cells. Data are mean ± s.d. (biologically triplicates of infected cells). **e**, Inhibitory efficacy of inhibitors against PSV entry of SARS-CoV-2-D614G, HKU1, HKU3 and HKU5 in HEK293T cells stably expressing the indicated CVRs. Data are mean ± s.d. (biologically triplicates of infected cells), representative of two infection inhibition assays with similar results. *P < 0.05, **P < 0.01, ***P < 0.001, ****P < 0.0001; NS, Not significant (P > 0.05).



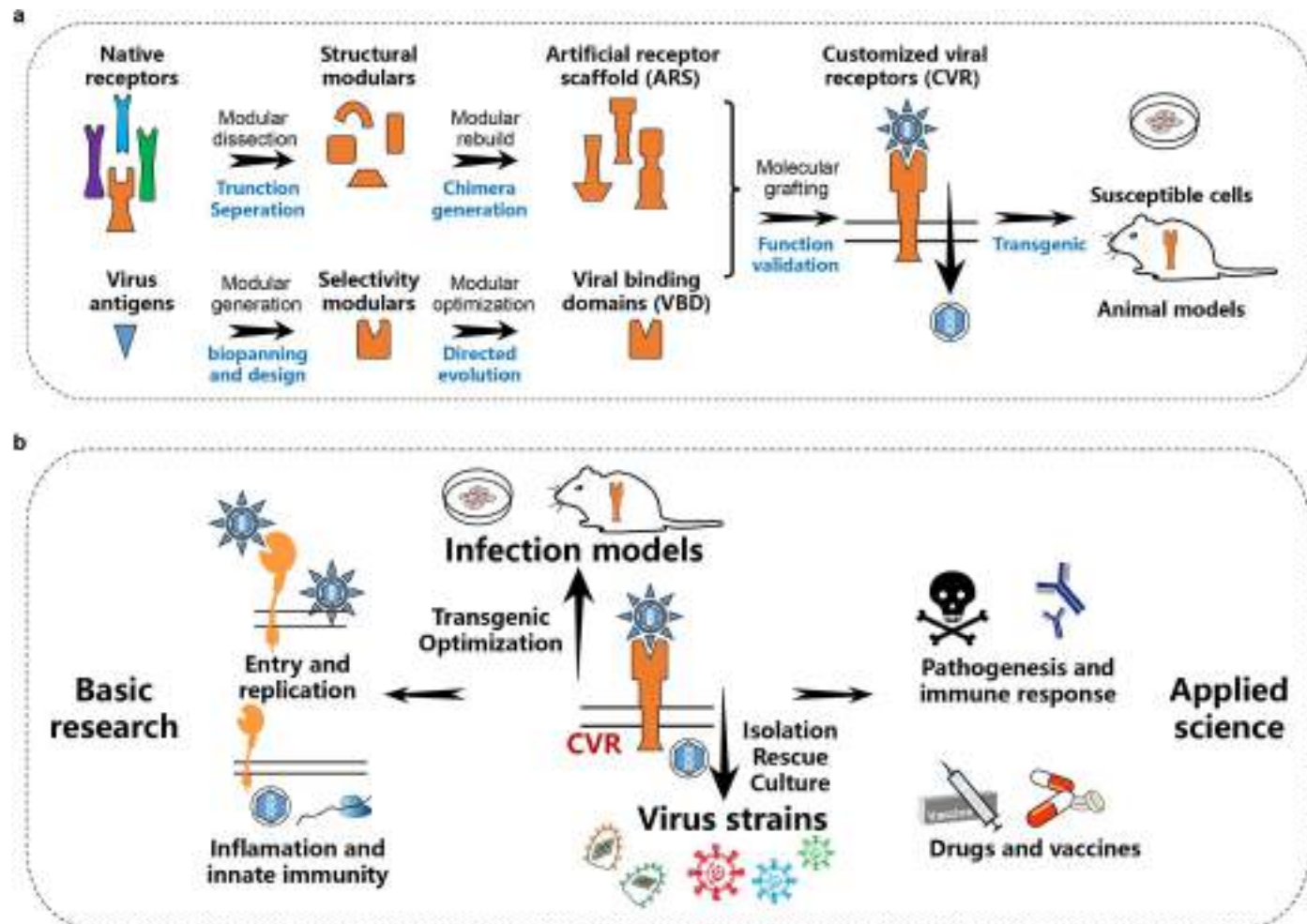
Extended Data Fig. 10 | See next page for caption.

Article

Extended Data Fig. 10 | Characterization of CVR-promoted amplification of replication-competent pcVSV-CoVs or authentic coronaviruses.

a, Genetic organizations and workflow for generating replicable pcVSV-HKU3 or pcVSV-HKU5. **b**, Successful rescue (P0) and amplification (P1) of pcVSV-HKU3 assisted by VSV-G. Representative images of an experiment that was conducted for a single time. **c**, **d**, Trypsin-enhanced cell-cell fusion (**c**) and VSV-G-independence (**d**) of pcVSV-HKU3 infection in Caco2-Nb27 (MOI: 0.001). Data are representative of four independent infection assays with similar results. **e**, **f**, Accumulation of pcVSV-HKU3 (**e**) or pcVSV-HKU5 (**f**) RNA copies in the supernatant at indicated time points. **g**, pcVSV-HKU5 mediated cell-cell fusion in Caco2 or Caco2-1B4 cells at MOI = 0.1. TPCK-Try + : 20 µg ml⁻¹ TPCK-treated Trypsin in DMEM + 2% FBS. Representative of two independent experiments. **h**, TCID₅₀ determination assay for RsHuB2019A in Caco2-Nb27 cells by the Red-Muench method. Caco2-Nb27 cells were inoculated with a 10-fold serial dilution of RsHuB2019A containing supernatant (Passage 6). The TCID₅₀ was determined using immunofluorescence to detect the presence of N protein expression of the inoculated cells at 4 dpi. **i**, Trypsin-dependent amplification of RsHuB2019A in Huh-7 cells. The RsHuB2019A genomic RNA copies in the supernatant collected at indicated time points of infected Huh-7 cells were quantified by RT-qPCR using RdRp-specific primers. Inoculation was conducted at an MOI of 0.0001, with or without trypsin treatment. Try: 100 µg ml⁻¹ Trypsin in DMEM. **j**, Genetic organizations of the HKU5 (HKU5-1LMH03f) ΔORF5-ZsGreen-HiBit (HKU5-ZGH). **k-m**, Supernatant RNA copies of HKU5-ZGH (**k**) in Caco2-1B4 cells, ZsGreen-HiBit signal (**l**), and increase in ZsGreen intensity (PO) (**m**). Representative of two independent infection assays are shown. Data

are mean ± s.d. ($n = 3$ independently infected wells of cells) for **l**. **n**, Isolation of HKU5 (strain PaGD2014/15) from bat samples by Caco2-1B4 cells and its trypsin-dependent propagation. **o**, Vero E6 and Caco2 cells were infected with HKU5-1 (LMH03f) with or without trypsin treatment. Data are representative of three independent experiments. **p**, Sequencing results show L76R and K519T mutations in HKU5 spikes after ten passages in Caco2-1B4 cells. **q**, HKU5-1 after ten passages carrying mutations remains unable to infect Caco2 cells without exogenous trypsin treatment. Caco2-1B4 with CVR expression was included as a positive control. **r**, Efficacy of indicated antiviral reagents against HKU5-1 infection in Caco2-1B4 cells assessed by intracellular N proteins at 48 hpi. **s**, Efficient inhibition of HKU5 entry by EK1 and EK1C4 peptides in Caco2-1B4. **t**, Inhibitory effect of selected anti-viral reagents against authentic HKU5-ZGH infection in Caco2-1B4. Inhibitors were coincubated with either the cells or the viruses for 1 h and present in the culture medium during infection. The HiBiT-based luciferase activity was determined at 48 hpi to assess the inhibitory effect of selected anti-viral reagents against the infection of authentic HKU5-ZGH in Caco2-1B4. Data are representative of two independent infection assays for **r-t**. **u**, Overview of the protease cleavage sites of selected coronaviruses. The residue responsible for reduced endosomal cysteine protease activity (ECP) is marked in red, numbering based on SARS-CoV-2. The HKU5 infection efficiencies in **n**, **o**, **q**, **r**, and **s** were assessed using rabbit polyclonal antibodies targeting the HKU5 N protein (Cy3) at 48 hpi. Data presented are RNA copies of two independently infected cells with each point representing the mean of technical duplicates (RT-qPCR) for **e**, **f**, **i**, and **k**, representative of two independent experiments. Scale bars: 125 µm for all images.



Extended Data Fig. 11 | Schematic diagram of the modular design strategy for CVRs and the potential applications of this technique. a, Workflow outlining the process of creating artificial receptor scaffolds (ARS) and viral binding domains (VBDs) to construct functional customized viral receptors

(CVRs) for establishing in vitro and in vivo infection models. **b,** The crucial role of CVRs in bridging infection models and virus strains, along with the potential applications of this technique in both basic research and applied science.

Article

Extended Data Table 1 | CryoEM data collection, processing, and model refinement statistics

Data collection and processing		
Magnification (nominal)	130,000	
Voltage (kV)	300	
Electron exposure (e ⁻ /Å ²)	63	
Defocus range (μm)	0.3-2.0	
Pixel size (Å)	0.843	
Processing type	Global	Local
Symmetry imposed	C3	none
Initial particle images (no.)	381,075	497,199
Final particle images (no.)	165,733	209,164
Map resolution (Å)	2.6	3.2
FSC threshold	0.143	0.143
Map sharpening <i>B</i> factor (Å ²)	85.7	114.8
Refinement		
Initial model used (PDB code)	7LXY	7SOB
Model resolution (Å)	2.8	3.4
FSC threshold	0.5	0.5
Model composition		
Nonhydrogen atoms	26,337	4006
Protein residues	3,768	496
Glycan residues	60	9
<i>B</i> factors (Å ²)		
Protein	34.9	17.0
Glycans	22.7	21.9
R.m.s. deviations		
Bond lengths (Å)	0.01	0.01
Bond angles (°)	1.03	1.03
Validation		
MolProbity score	0.8	0.7
Clashscore	0.83	0.26
Rotamer outliers (%)	0.3	0.0
Privateer glycan issues (%)	0.0	0.0
Ramachandran plot		
Favored (%)	98.0	97.5
Allowed (%)	2.0	2.5
Outliers (%)	0.0	0.0
EMRinger score	4.9	5.1
Data Availability		
EMDB	EMD-45174	EMD-45175

Corresponding author(s): Huan Yan

Last updated by author(s): Aug 21, 2024

Reporting Summary

Nature Portfolio wishes to improve the reproducibility of the work that we publish. This form provides structure for consistency and transparency in reporting. For further information on Nature Portfolio policies, see our [Editorial Policies](#) and the [Editorial Policy Checklist](#).

Statistics

For all statistical analyses, confirm that the following items are present in the figure legend, table legend, main text, or Methods section.

n/a Confirmed

- The exact sample size (n) for each experimental group/condition, given as a discrete number and unit of measurement
- A statement on whether measurements were taken from distinct samples or whether the same sample was measured repeatedly
- The statistical test(s) used AND whether they are one- or two-sided
Only common tests should be described solely by name; describe more complex techniques in the Methods section.
- A description of all covariates tested
- A description of any assumptions or corrections, such as tests of normality and adjustment for multiple comparisons
- A full description of the statistical parameters including central tendency (e.g. means) or other basic estimates (e.g. regression coefficient) AND variation (e.g. standard deviation) or associated estimates of uncertainty (e.g. confidence intervals)
- For null hypothesis testing, the test statistic (e.g. F , t , r) with confidence intervals, effect sizes, degrees of freedom and P value noted
Give P values as exact values whenever suitable.
- For Bayesian analysis, information on the choice of priors and Markov chain Monte Carlo settings
- For hierarchical and complex designs, identification of the appropriate level for tests and full reporting of outcomes
- Estimates of effect sizes (e.g. Cohen's d , Pearson's r), indicating how they were calculated

Our web collection on [statistics for biologists](#) contains articles on many of the points above.

Software and code

Policy information about [availability of computer code](#)

Data collection

The Western blot data are collected by ChemiDoc MP Imaging System (Bio-Rad). Luciferase activity was measured using the Spectra Max iD3 multi-well Luminometer (Molecular Devices, United States), GloMax® 20/20 Luminometer (Promega, United States), or Varioskan LUX Multi-well Luminometer (Thermo Fisher). Flow cytometry data were generated using the CytoFLEX Flow Cytometer (Beckman Coulter, United States). BLI assays were conducted on an Octet RED96 instrument (Molecular Devices, United States). Fluorescent images were captured with either the MI52-N fluorescence microscope (Mshot) or the EVOS M5000 fluorescence microscope (Thermo Fisher Scientific). qRT-PCR was conducted using the C1000 Touch Thermal Cycler/CFX96 Real-time system (Bio-Red). For electron microscope analysis of negatively stained virion, images were collected at 200 kV using a Tecnai transmission electron microscope (FEI). For antibody-triggered S refolding assay, micrographs were recorded using the Leginon software (version 3.1) on a 120 kV FEI Tecnai G2 Spirit with a Gatan Ultrascan 4000 4k x 4k CCD camera. For cryoEM analysis of S2L20 and SARS-CoV-2 spike related structures, micrographs were collected using the Leginon software(version 3.1) to control a FEI Titan Krios transmission electron microscope (Thermo Fisher) equipped with a K3 direct detector (Gatan, Pleasanton, CA) and operated at 300 kV with a Gatan Quantum GIF energy filter.

Data analysis

GraphPad Prism (version 8.0.2) was used for all statistical analyses. Image Lab 5.2.1 was utilized to analyze Western blot data. FlowJo (version 10) was employed for the analysis of flow cytometry data. Protein sequence alignment was performed using the Mafft (version 7.313) and Geneious Prim (version 2023.0.1). Phylogenetic analysis was performed using the IQ-Tree (version v.2.0.8) and rendered with iTOL (version 6) (<http://itol.embl.de>). Protein structures were presented and analyzed using UCSF ChimeraX (version 1.7.1). Octet Data Analysis software (version v.12.2.0.20) was used for the analysis of BLI data. The Bio-Rad CFX Maestro (version 4.1.2433.1219) was employed for the analysis of Real-time PCR data. The raw data of the Cryo-EM were processed by MotionCor2 (version 1.3.0); the defocus value for each micrograph was determined using Gctff; the preprocessing was done using Warp (version 1.0.9). The well-defined partial particles were selected for initial model reconstruction in Relion (version 3.0) and final reconstructions used either Relion (version 3.0) or cryoSPARC (version 3.3.1). Local resolution was evaluated using ResMap (version 1.95) or cryoSPARC(version 3.3.1). The protein complex structures were manually built into

the refined maps in Coot (version 0.9.4), UCSF Chimera (version 1.15), or UCSF ChimeraX (version 1.1). The model was then refined and rebuilt into the map using Coot (version 0.9.4), Rosetta (version 1.2.5), and ISOLDE(version 1.6). Model validation and analysis used MolProbity, EMRinger, Privateer, and Phenix (version 1.19). Figures were generated using UCSF ChimeraX (version 1.1).

For manuscripts utilizing custom algorithms or software that are central to the research but not yet described in published literature, software must be made available to editors and reviewers. We strongly encourage code deposition in a community repository (e.g. GitHub). See the Nature Portfolio [guidelines for submitting code & software](#) for further information.

Data

Policy information about [availability of data](#)

All manuscripts must include a [data availability statement](#). This statement should provide the following information, where applicable:

- Accession codes, unique identifiers, or web links for publicly available datasets
- A description of any restrictions on data availability
- For clinical datasets or third party data, please ensure that the statement adheres to our [policy](#)

The CryoEM maps and models have been deposited to the Electron Microscopy Data Bank and Protein Data Bank (PDB) with accession numbers EMD-45174/PDB ID 9C44 (global refinement of the S2L20-bound S trimer) and EMD-45175/PDB ID 9C45 (local refinement of the NTD and S2L20 Fab variable region) . The accession numbers (NCBI GenBank or GISAID), and protein sequence information of receptor, virus, antibody, domains, and reporter genes are provided in the Methods and Supplementary Tables. All other data supporting the findings of this study are available with the Article and the Supplementary Information. Source data are provided with this paper.

Research involving human participants, their data, or biological material

Policy information about studies with [human participants or human data](#). See also policy information about [sex, gender \(identity/presentation\), and sexual orientation](#) and [race, ethnicity and racism](#).

Reporting on sex and gender

The sex and gender are not relevant to the goal of this experiment, which aims to compare the neutralizing profile based on two different infection models, ACE2 or CVR. We utilized the available sera from 20 individuals as reagents, all of whom had previously verified neutralizing activity.

Reporting on race, ethnicity, or other socially relevant groupings

All sera samples were collected from individuals of East Asian (Chinese) background.

Population characteristics

The vaccinated sera were collected from volunteers approximately 21 days following the third dose of the WHO-approved inactivated SARS-CoV-2 vaccine (CorovaVac, Sinovac, China). Median age of volunteers was 37 years, with 44% being male and 56% female.

COVID-19 convalescents from ten communities in five different streets (Chezhan Street, Danshuichi Street, Huaqiao Street, Yiyuan Street, and Dazhi Street) in Jiang'an District in Wuhan, whose symptom onset was between January 1, 2020, and March 26, 2020, were randomly recruited to the cohort according to the principle of the easy sampling. Convalescents with mental disorders, dementia, difficulty in moving freely, refused to enroll, or not reachable were excluded from the cohort.

Recruitment

The vaccinated sera volunteers were recruited by Sinovac, Inc. None of the participants had a history of prior SARS-CoV-2 infection, and none reported serious adverse events after vaccination. The convalescents were randomly recruited to the cohort with symptom onset between January 1, 2020, and March 26, 2020. All volunteers were provided informed written consent forms, and the whole study was conducted following the requirements of Good Clinical Practice of China.

Ethics oversight

Ethical approval for the vaccinated individuals was granted by the Ethics Committee (seal) of Beijing Youan Hospital, Capital Medical University, with approval number LL-2021-042-K. The collection of sera from Wuhan COVID-19 convalescents was conducted in collaboration with the Hubei Provincial Center for Disease Control and Prevention and Hubei Provincial Academy of Preventive Medicine (HBCDC), following written consent and under the approval of the Institutional Review Boards with the identification number 2021-012-01.

Note that full information on the approval of the study protocol must also be provided in the manuscript.

Field-specific reporting

Please select the one below that is the best fit for your research. If you are not sure, read the appropriate sections before making your selection.

Life sciences Behavioural & social sciences Ecological, evolutionary & environmental sciences

For a reference copy of the document with all sections, see nature.com/documents/nr-reporting-summary-flat.pdf

Life sciences study design

All studies must disclose on these points even when the disclosure is negative.

Sample size

CVRs were designed for 14 representative coronaviruses, selected from six different subgenera, with notable diversity in their receptor-binding domains across the Coronaviridae. This selection sufficiently demonstrates the generalizability of CVR among coronaviruses (Fig.4a and

Supplementary Table 1). To identify the optimal trans-membrane motif (TM) for CVR design, we tested thirty-one TM sequences from various receptors (Extended Data Fig.1). Considering the overall hydrophobic nature of TM sequences, the 31 variable sequences are sufficient to illustrate the impact of TM optimization on CVR functionality. To identify acceptable VBD epitopes for CVR design, we assessed twenty-two SARS-CoV-2 neutralizing antibodies from 13 different epitopes on the SARS-CoV-2 spike for their entry-supporting ability (Fig.2a). These 22 selected antibodies cover most known neutralizing epitopes and provide comprehensive and meaningful data in this mapping assay. Ten serum samples from vaccinated individuals and ten serum samples from COVID-19 convalescents were analyzed to compare the neutralizing activities between native receptor-based infection system and CVR-based infection system (Extended Data Fig.9). The focus of this experiment is to compare the overall neutralization profile using all our available samples as reagents. It showed that the data from these 20 sera samples are enough for us to draw a conclusion about the difference of the two infection models (Extended data Fig.20).

Data exclusions	There is no data excluded from the analysis.
Replication	The majority of experiments were conducted 2 to 4 times, with 2 to 4 biological replicates (most are triplicated), each yielding similar results.
Randomization	Our rationale in these experiments is to test as many sequences/sera samples as we can to gather data to support the conclusion of a proof of concept study. Consequently, we test all available sequences/samples and randomization was not conducted based our experimental design.
Blinding	No grouping is applied in this study. Therefore blinding is not applicable here.

Reporting for specific materials, systems and methods

We require information from authors about some types of materials, experimental systems and methods used in many studies. Here, indicate whether each material, system or method listed is relevant to your study. If you are not sure if a list item applies to your research, read the appropriate section before selecting a response.

Materials & experimental systems		Methods	
n/a	Involved in the study	n/a	Involved in the study
<input type="checkbox"/>	<input checked="" type="checkbox"/> Antibodies	<input checked="" type="checkbox"/>	ChIP-seq
<input type="checkbox"/>	<input checked="" type="checkbox"/> Eukaryotic cell lines	<input type="checkbox"/>	<input checked="" type="checkbox"/> Flow cytometry
<input checked="" type="checkbox"/>	<input type="checkbox"/> Palaeontology and archaeology	<input checked="" type="checkbox"/>	<input type="checkbox"/> MRI-based neuroimaging
<input type="checkbox"/>	<input checked="" type="checkbox"/> Animals and other organisms		
<input checked="" type="checkbox"/>	<input type="checkbox"/> Clinical data		
<input checked="" type="checkbox"/>	<input type="checkbox"/> Dual use research of concern		
<input checked="" type="checkbox"/>	<input type="checkbox"/> Plants		

Antibodies

Antibodies used	<p>Primary antibodies:</p> <ol style="list-style-type: none"> Commercial: <p>Monoclonal ANTI-FLAG® M2, Mouse mAb, clone M2, Cat: F1804-1MG, Lot: SLCF4933, Sigma-Aldrich, (WB, 1:10,000; IFA, 1:1,000); ANTI-FLAG Tag mAb, Rabbit mAb, clone D6W5B, Cat: 14793S, Lot: 7, Cell Signaling Technology (CST), (Flow Cyt, 1:1000); SARS-CoV/SARS-CoV-2 Nucleocapsid Antibody, Mouse mAb, Clone #05, Cat: 40143-MM05, Lot: HB14JU1205, Sino Biological, (IFA, 1:10,000); Anti-HA-tag mAb, Mouse mAb, Clone TANA2, Cat: M180-3, Lot: 012, MBL, (WB, 1:5,000); β-Tubulin Monoclonal Antibody(5G3), Mouse mAb, clone 5G3, Cat: YM3030, Lot: B3001, Immunoway, WB, 1:10,000); Anti-VSV-M [23H12] Antibody, Mouse mAb, Clone 23H12, Cat: EB0011, Lot: 200826, Kerafast, (WB, 1:10,000); GAPDH Polyclonal Antibody, Rabbit pAb, Polyclonal Antibody, Cat: ANT325, Lot: 32151127, AntGene, (WB, 1:10,000);</p> Non-commercial: <p>(lab produced as recombinant proteins or as sera collected from immunized rabbits).</p> <ul style="list-style-type: none"> (a) Monoclonal recombinant proteins: <p>Stem-helix-S2P6 monoclonal antibody, Human mAb: S2P6; PMID: 34344823 (WB: 1 µg/mL); MHV-A59 Spike-targeting (1F7-mFc), nanobodies fused with mouse Fc, (IFA, 1 µg/mL)</p> 229E-VR740 Spike-targeting (1A1-mFc), nanobodies fused with mouse Fc, (IFA, 1 µg/mL) Anti-SARS-CoV-2 S2 antibody (76E1), Human mAb, (Flow cytometry: 1 µg/mL); <ul style="list-style-type: none"> (b) Polyclonal sera: <p>Polyclonal rabbit anti-SARS-related CoV Rp3 N protein serum (IFA, 1:2000); cross-reactive with RSVB2019A N protein, PMID: 37655938 (IFA, 1:4000); Polyclonal rabbit anti-HKU5 N protein serum, (IFA, 1:4000);</p> Secondary antibodies: <p>(a) HRP conjugated: <p>Anti-Human IgG (Fc specific) Peroxidase antibody produced in goat, Cat: A0170-1ML, Lot: 0000088197, Sigma-Aldrich, (WB, 1:5,000); Goat Anti-Rabbit IgG-Fc Secondary Antibody (HRP), Cat: SSA003, Lot: HO13AU0906, Sino Biological, (WB, 1:5,000); Peroxidase AffiniPure™ Goat Anti-Mouse IgG (H+L), Cat: 115-035-003, Lot: 143988, Jackson Lab, (WB, 1:5,000);</p> </p> (b) Fluorescence labeled:
-----------------	---

Goat anti-Mouse IgG (H+L) Highly Cross-Adsorbed Secondary Antibody, Alexa Fluor™ Plus 488, Cat: A32723, Lot: XH353656, Thermo Fisher Scientific, (IFA, 1:1,000; Flow Cyt, 1:5000);
 Goat anti-Mouse IgG (H+L) Highly Cross-Adsorbed Secondary Antibody, Alexa Fluor™ Plus 594, Cat: A32742, Lot: XH353664, Thermo Fisher Scientific, (IFA, 1:1,000; Flow Cyt, 1:5000);
 Goat anti-Human IgG (H+L) Cross-Adsorbed Secondary Antibody, Alexa Fluor™ 488, Cat: A11013, Lot: 2747411, Thermo Fisher Scientific, (IFA, 1:1,000; Flow Cyt, 1:5000);
 Goat anti-Human IgG Fc Cross-Adsorbed Secondary Antibody, DyLight 594, Cat: SA5-10136, Lot: VI3076647, Thermo Fisher Scientific, (IFA, 1:1,000; Flow Cyt, 1:5000);
 Goat anti-Rabbit IgG (H+L) Highly Cross-Adsorbed Secondary Antibody, Alexa Fluor™ Plus 647, Cat: A32733, Lot: VH308578A, Thermo Fisher Scientific, (IFA, 1:1,000; Flow Cyt, 1:5000);
 Goat anti-Mouse IgG (H+L) Highly Cross-Adsorbed Secondary Antibody, Alexa Fluor Plus 647, Cat: A32728, Lot: VB297823, Thermo Fisher Scientific, (IFA, 1:1,000; Flow Cyt, 1:5000);
 Goat Anti-Rabbit IgG H&L (Cy3 ®) preadsorbed, Cat: ab6939, Lot: GR3174210-9, abcam, (IFA, 1:250);

4. Neutralizing antibodies:

(Note: All these neutralizing antibodies are lab-produced as recombinant proteins through transfection of plasmids into HEK293T cells except for the Anti-VSV-G which is purified from the Hybridoma supernatant.)

(a) Anti SARS-CoV-2 Spike:

S2P6, Human mAb: S2P6 (PMID: 34344823); B6, Human mAb: B6 (PMID: 33981021); 76E1, Human mAb: 76E1 (PMID: 35773398); S2L20, Human mAb: S2L20 (PMID: 33761326); CB6, Human mAb: CB6 (PMID: 32454512); REGN, Human mAb: REGN (PMID: 32540901); LY-COV555, Human mAb: LY-COV555 (PMID: 33024963); S309, Human mAb: S309 (PMID: 32991844); S2H97, Human mAb: S2H97 (PMID: 34261126); S2X259, Human mAb: S2X259 (PMID: 34261126); S2M11, Human mAb: S2H97 (PMID: 32972994); BG10-19, Human mAb: BG10-19 (PMID: 34015271).

(b) Anti-human ACE2H11B11: Human mAb: H11B11 (PMID: 34404805);

(c) Anti-VSV-G: Mouse mAb ATCC, I1-Hybridoma (CRL-2700) cell line.

The detailed antibody/nanobody informations can be found in the Supplementary Table 3.

Validation

Validation for commercial primary antibodies:

Mouse anti-FLAG® mAb, M2 Sigma-Aldrich (WB, 1:10,000; IFA, 1:1,000). Vendor validated highly sensitive and specific detection of FLAG fusion proteins by WB/IP/IHC/IF/ICC. Optimized for single banded detection of FLAG fusion proteins in mammalian, plant, and bacterial expression systems.

<https://www.sigmaldrich.cn/CN/en/product/sigma/f1804>

Rabbit anti-FLAG mAb D6W5B, CST, (FCM, 1:1000). Binds to epitope as Sigma-Aldrich Anti-FLAG M2 antibody. Vendor validated application for WB/IP/IHC/IF/FCM in HEK293T cells.

<https://www.cellsignal.cn/products/primary-antibodies/dykdddktag-d6w5b-rabbit-mab-binds-to-same-epitope-as-sigma-aldrich-anti-flag-m2-antibody/14793>

Mouse anti-SARS-CoV-2 Nucleocapsid mAb, Clone #05, Sino Biological, (IFA, 1:10,000); Vendor validated application for WB/ELISA/IHC/FCM.

<https://www.sinobiological.com/antibodies/cov-nucleocapsid-40143-mm05>

Mouse anti-HA mAb, MBL, (WB, 1:5,000); Vendor validated application for WB/IP/FCM/FCM.

<https://www.mblbio.com/bio/g/dtl/A/?pcd=M180-3>

Mouse anti β-Tubulin mAb (5G3), Immunoway, (WB, 1:10,000). Vendor validated application for WB/IF/IHC. Reactive with β-Tubulin from different species (Human/Rat/Mouse/Mk/Dg/Ch/Hamster/Rabbit/sheep)

<http://www.biowellway.com/CHome/22/YM3030>

Mouse anti-VSV-M [23H12] Kerafast, (WB, 1:10,000); Vendor validated application for high sensitivity of WB detection of VSV-M.

<https://www.kerafast.com/productgroup/1011/anti-vsv-m-23h12-antibody?ProductID=445>

Rabbit anti-GAPDH pAb, AntGene, (WB, 1:10,000); Vendor validated application for WB/IP/IHC/IF. Reactive with GAPDH from different species (Human, Mouse, Rat, Pig, Arabidopsis, Corn, Cabbage, Rice)

<http://www.antgene.org/ANT325%20GAPDH%20Polyclonal%20Antibody.pdf>

HRP and Fluorescence labeled Commercial secondary antibodies were validated by the vendor for applications of WB and IF/FCM, respectively.

Non-commercial primary antibodies were all produced in the lab with sequence and protein expression verified. The application of these antibodies were either validated by the indicated papers (with PMID) for initial report or with data provided in this paper. The list include:

Human anti-SARS-CoV-2 mAb: S2P6 (WB: 1 µg/mL) (PMID: 34344823)

MHV-A59 Spike-targeting (1A1-mFc), nanobodies fused with mouse Fc, (IFA, 1 µg/mL) Validated with data this paper.

229E-VR740 Spike-targeting (1F7-mFc), nanobodies fused with mouse Fc, (IFA, 1 µg/mL) Validated with data this paper.

Anti-SARS-CoV-2 S2 antibody (76E1), Human mAb, (FCM: 1 µg/mL); (PMID: 35773398) and also validated with data this paper.

Polyclonal Rabbit anti-SARS-related CoV Rp3 N protein serum (IFA, 1:2000); cross-reactive with RSVB2019A N protein, (PMID: 37655938) (IFA, 1:4000); and also validated with data in this paper.

The specificity of S2P6 for Western blotting (WB) was validated in 293T cells. The specificity of rabbit anti-HKU5 N protein serum for immunofluorescence analysis (IFA) was lab-verified in Caco2 and Vero-E6 cell lines. The specificity of 1A1-mFc and 1F7-mFc for IFA were lab-verified in 293T and BHK-21 cells. The specificity of 76E1 for flow cytometry was verified in 293T cells.

Non-commercial neutralizing antibodies used in this study were all produced in the lab with sequence and protein expression verified. All these antibodies were validated by the indicated papers (with PMID) for initial report and data provided in this paper. The list include:

H11B11 (PMID: 34404805), B6 (PMID: 33981021), S2P6 (PMID: 34344823), 76E1 (PMID: 35773398), S2L20 (PMID: 33761326); CB6 (PMID: 32454512); REGN (PMID: 32540901); LY-COV555 (PMID: 33024963); S309 (PMID: 32991844); S2H97 (PMID: 34261126); S2X259 (PMID: 34261126); S2H97 (PMID: 32972994); BG10-19 (PMID: 34015271), and Rp3 N protein antiserum (PMID: 37655938).

Eukaryotic cell lines

Policy information about [cell lines and Sex and Gender in Research](#)

Cell line source(s)	HEK293T (CRL-3216), Vero E6 cells (CRL-1586), A549 (CCL-185), BHK-21 (CCL-10), Caco2 (HTB-37), Neuro2a (CCL-131), Tb 1 Lu (CCL-88), and I1-Hybridoma (CRL-2700) were purchased from ATCC. Huh-7 (SCSP-526) cells were purchased from the Cell Bank of Type Culture Collection, Chinese Academy of Sciences.
Authentication	Not authenticated.
Mycoplasma contamination	Cell lines used in this study were not tested for mycoplasma contamination.
Commonly misidentified lines (See ICLAC register)	No commonly misidentified line was used.

Animals and other research organisms

Policy information about [studies involving animals; ARRIVE guidelines](#) recommended for reporting animal research, and [Sex and Gender in Research](#)

Laboratory animals	This study did not involve laboratory animals.
Wild animals	Pipistrellus abramus bats were captured in Guangzhou City, Guangdong province on June 28, 2014, which were trapped from their natural habitat by fishing nets placed at the entrance of known bat roosting caves. Adult bats were sampled and the age information of these bats was not collected. All bats trapped for this study were immediately released back to their habitat without transportation after anal swab collection.
Reporting on sex	Information of sex was not collected.
Field-collected samples	The anal swabs were collected and preserved in viral transport medium (VTM) comprising Hank's balanced salt solution, BSA (1%), amphotericin (15 µg/mL), penicillin G (100 U/ml), and streptomycin (50 µg/mL) (PMID:24172901), transported to the laboratory and stored at -80°C until use. All members of field teams wore appropriate personal protective equipment, including N95 masks, tear-resistant gloves, disposable outerwear, and safety glasses.
Ethics oversight	All sampling processes were carried out by veterinarians with approval from the Animal Ethics Committee of the Wuhan Institute of Virology (WIVH05210201).

Note that full information on the approval of the study protocol must also be provided in the manuscript.

Plants

Seed stocks	n/a
Novel plant genotypes	n/a
Authentication	n/a

Flow Cytometry

Plots

Confirm that:

- The axis labels state the marker and fluorochrome used (e.g. CD4-FITC).
- The axis scales are clearly visible. Include numbers along axes only for bottom left plot of group (a 'group' is an analysis of identical markers).
- All plots are contour plots with outliers or pseudocolor plots.
- A numerical value for number of cells or percentage (with statistics) is provided.

Methodology

Sample preparation

For flow cytometry analysis, viral antigen-mFc and VBDs-mFc recombinant proteins were diluted in DMEM at the indicated concentrations and then incubated with HEK293T cells expressing the indicated receptors or coronaviruses spike proteins for 1 hour at 37°C. In live cell binding assays, for detecting the cell surface hFc or intracellular ZsGreen, cells were washed with DMEM and subsequently incubated with either Alexa Fluor 594-conjugated goat anti-mouse IgG (Thermo Fisher Scientific; A32742) or a combination of Alexa Fluor 488-conjugated goat anti-human IgG (Thermo Fisher Scientific; A11013). In live cell binding assays, for detecting the cell surface 76E1 epitope exposure, the SARS-CoV-2-S IRES-ZsGreen expressing cells were incubated with indicated concentrations of scFv-mFc or soluble receptors for 1 hour at 37°C before 76E1 antibody incubation (1 µg/mL). When detection of the intracellular FLAG tag is necessary, cells were washed once with HBSS and fixed with 4% PFA, permeabilized with 0.1% Triton X-100, blocked with 1% BSA/PBS at 4°C for 30 minutes, and subsequently stained with Rabbit anti-Flag tag mAb (CST,14793S) diluted in 1% BSA/PBS for 1 hour at 4°C to visualize the expression of CVRs and other receptors. Following extensive washing, the cells were incubated with Alexa Fluor 647-conjugated goat anti-rabbit IgG (Thermo Fisher Scientific; A32733) and Alexa Fluor 488-conjugated goat anti-mouse IgG (Thermo Fisher Scientific; A32723), both diluted in 1% BSA/PBS, for 1 hour at 4°C. Subsequently, flow cytometry analysis was performed using a CytoFLEX analyzer. No sorting was conducted in this study.

Instrument

CytoFLEX Flow Cytometer (Beckman Coulter, United States).

Software

FlowJo version 10

Cell population abundance

Only HEK293T cells were used in the Flow Cytometry analysis and no sorting was conducted in this study. 5,000 events in the gated area were analyzed for all samples.

Gating strategy

20,000-50,000 events without gating were recorded for all samples. Gating was initially performed to exclude cell debris and dead cells (FSC-H/SSC-H) for subsequent analysis (P1). Secondary gating, based on FLAG/hFc/ZsGreen-positive cells, was then conducted to distinguish cells expressing detectable receptors/spike proteins (P2). Gating thresholds were established using histogram profiles of mock controls, which consisted of HEK293T cells transfected with empty vector plasmids or non-relevant receptor plasmids. Subsequently, 5,000 events within the P2 population were recorded for binding efficiency analysis.

- Tick this box to confirm that a figure exemplifying the gating strategy is provided in the Supplementary Information.